Interferometric Phase of Clutter-Suppression Residuals Aided Multichannel SAR-GMTI

Min Tian, *Member, IEEE*, Bin Liao, *Senior Member, IEEE*, Bo Yuan, *Senior Member, IEEE*, Deng Hui Hu

***Abstract*—For multichannel synthetic aperture radar (SAR) ground moving target identification (GMTI) in heterogeneous and strong clutter backgrounds, it is challenging to accurately detect slow and weak targets when relying solely on the magnitude of clutter-suppression residuals, due to the significant clutter residuals and signal-to-noise losses. To address this, a detector that leverages both the magnitude and phase information in multichannel SAR-GMTI clutter suppression is proposed. For a M-channel SAR system, the detection test is formulated as the product of the residual magnitude from M-channel clutter suppression and a phase factor derived from the interferometric phase between two residuals from the first and last $M-1$ channels. This phase factor captures the dissimilarity from the clutter, enabling the suppression of strong clutter residuals and improving the signal-to-clutter-plus-noise ratio (SCNR). Using the product clutter model, a constant false alarm ratio detection framework is designed. The receiver operator characteristic metrics, obtained from simulations and real-data experiments, validate the proposed method's superiority over the state-of-the-art techniques, and the detection sensitivity on the clutter heterogeneity, correlation coefficients between pairs of clutter-suppression residuals, and target parameters is analyzed for practicality. In the X-band airborne radar GMTI experiments, the minimum discernible input SCNR of -6 dB for target radial velocity of 4 m/s and 0 dB for 2 m/s demonstrate the effectiveness in detecting the dim targets within strong clutter.**

***Index Terms*—Multichannel synthetic aperture radar (SAR), slow and weak target detection, clutter residual suppression, joint detection metric.**

I. Introduction

SYnthetic aperture radar (SAR) systems mounted on the aircraft or spacecraft typically use an antenna array with multiple phase centers to suppress ground clutter and improve the signal-to-clutter-plus-noise ratio (SCNR) for effective target detection in air-to-ground surveillance [1]–[3]. In practice, applying the clutter suppression such as the space-time adaptive processing (STAP) [2], and displaced phase center antenna (DPCA) often suffer from performance degradation due to various real-world factors including the system's non-linear response and registration errors [3], [4], the terrain's elevation and type variations [5], [6], and the clutter internal motions [7]. Consequently, undesired strong and isolated clutter residuals and significant target power losses may appear in the processed outputs [8], [9], posing challenge for accurately detecting the dim targets with the slow velocity and low signal-to-noise ratio (SNR) for ground moving target identification (GMTI), especially in heterogeneous clutter environments [10].

From the past few decades until now, various techniques have been continuously developed for enhancing clutter suppression performance in applications. For accurate estimation of the clutter-plus-noise covariance matrix (CCM) in adaptive clutter suppression processing, the sample selection algorithms based on spectral similarity [11], exploiting the digital terrain database [12], and using the machine learning approach [13] have been investigated to obtain the secondary samples that satisfy the independent and identically distributed (i.i.d.) condition with the cell under the test. While these methods are generally effective with sufficient clutter samples, their estimation performance can severely degrade in heterogeneous environments where ground clutter typically consists of backscatter types with variable reflectivity, and the i.i.d. samples are limited. Reducing the STAP processing dimensions can lower the sample requirements and thus considerably alleviate the challenge of obtaining i.i.d. samples [2], [14], [15]. However, in highly heterogeneous detection backgrounds such as urban areas [6], these methods may experience performance degradation due to the limited i.i.d. sample availability, potentially leading to increased false alarms due to isolated and strong clutter.

Techniques based on the sparse recovery theory [16]–[18] and matrix structure properties [19], [20] can improve the CCM estimation accuracy under limited sample conditions. Nevertheless, these methods often come with high computational complexities when applying to each pixel of SAR images for enhanced accuracy, posing limitations for real-time SAR-GMTI applications. Deep learning-based STAP methods [21]–[23] utilize neural networks to model the complex nonlinear mapping between observed data and the space-time spectra, enabling the precise reconstruction of the CCM given sufficient labeled training data samples. In most practical conditions that labeled training data samples are limited, the above methods may suffer from performance degradation due to overfitting of the model. Recently, semi-supervised learning-based SAR automatic target recognition (ATR) has

This work was supported in part by the National Natural Science Foundation of China under Grant 62301398; in part by the Guangdong Provincial Key Laboratory under Grant 2023B1212060076; and in part by the Key Research Program of Frontier Sciences from Chinese Academy of Sciences under Grant ZDRW-KT-2022-2. (*Corresponding author: Bin Liao.*)

Min Tian is with the Hangzhou Institution of Technology, Xidian University, Hangzhou 312000, China, and also with the Xidian University, Xi' an, 710071, China (e-mail: tianmin@xidian.edu.cn).

Bin Liao is with the State Key Laboratory of Radio Frequency Heterogeneous Integration, Shenzhen University, Shenzhen 518060, China, and also with Guangdong Provincial Key Laboratory of Intelligent Information Processing, Shenzhen University, Shenzhen 518060, China (e-mail: binliao@szu.edu.cn).

Bo Yuan is with the Research Institute of Tsinghua University in Shenzhen, Shenzhen 518057, China (e-mail: boyuan@ieee.org).

Deng Hui Hu is with the Innovation Academy for Microsatellites of Chinese Academy of Sciences, Shanghai, 201304, China (hudh@microsate.com).

received increasing attentions due to excellent feature learning capability with fewer labeled training data samples [24]–[26]. For instance, the SAR ATR method based on a Connfucius tri-learnin paradigm [26] can accurately identify the extended targets in single channel SAR images by learning from both good examples and bad examples. However, for small-size moving targets within dense clutter, it may be a challenge to annotate targets and train the model as the difference between the point targets of low SCNRs and isolated clutter is extremely small relying solely on the SAR image.

Despite the above practical implementation requirements, the afore-mentioned advanced clutter rejection methods, when combined with careful registration and calibration processing [27] on multichannel SAR data, can significantly enhance the SCNRs of moving targets in the output, thereby improving target detection performance. Since slowly moving targets often experience greater power losses during clutter suppression processing [8], [28], target detection methods solely based on the magnitude of residuals in clutter suppression [9], [10], [29], [30] may fail to achieve an acceptable minimum discernible velocity (MDV).

The along-track interferometric (ATI) phase, which is proportional to the line-of-sight velocity of the backscatter in SAR images [31]–[34], is often used to discriminate slow targets from the clutter for target detection [35], [36]. The two-stage detection method that combines the interferometric magnitude and phase of dual-channel SAR [35] and the constant false-alarm ratio (CFAR) detector based on a joint metric of the interferometry magnitude and phase [36] have achieved a reduced probability of false alarms (Pfa) and a smaller MDV in heterogeneous clutter backgrounds. Nevertheless, due to their limited clutter suppression abilities, the weak moving targets in a strong clutter background may experience degraded detection performance.

Recently, a series of two-step detectors combining the STAP and ATI techniques have been proposed [37]–[39], and achieved significant improvements for SAR-GMTI. In [37], [38], the first stage, typically involving a test based on the magnitude of residuals from multichannel clutter suppression, detects potential targets with a low target detection threshold. Then, the second stage further reduces false alarms, caused by large clutter residuals in heterogeneous clutter backgrounds, using dissimilar tests such as the ATI phase [37] and degree of radial-velocity consistency [38]. For weak targets with low SCNRs, as the ATI phase is easily interfered by strong clutter signals, the two-step method [37] tends to have a low probability of target detection (Pd). Additionally, a local-to-global detection scheme using a group of tests, including the multibaseline ATI phases for fully exploiting the spatial degrees of freedom (DoF) and the magnitude of clutter-suppression residuals, can achieve a smaller MDV in heterogeneous clutter backgrounds [39]. However, the limitations of ATI phases for low-SCNR targets may restrict the detection capacity for weak targets under a strong clutter background. In contrast, the degree of radial-velocity consistency [38] exploiting the interferometric phase information between two clutter suppression residuals, respectively outputted from DPCA in the datasets before and after two channels, helps to mitigate clutter interferences for low-SCNR targets. Whereas, this metric focuses on the radial-velocity consistency across multiple pixels, and fails to detect the small-size targets that occupy fewer pixels in SAR images.

In this paper, an interferometric phase of clutter-suppression residuals aided multichannel SAR-GMTI method is proposed to enhance detection performance of dim targets against strong and heterogeneous clutter backgrounds. Assumes that an airborne SAR deploys M channels along the track direction and works in the side-looking mode. The proposed detector integrates the magnitude of the output from M-channel clutter suppression with the interferometric phase between two residuals, accounting for the clutter suppression in the datasets of before and after $M-1$ channels, respectively. Note that the interferometric phase between two residuals can achieve more accurate estimation results for the targets with low SCNRs over the classical ATI phase [37], [39], owing to the anti-clutter ability during the phase measurements. By leveraging both the magnitude and phase information of the residuals, the proposed method significantly suppresses large and strong clutter residuals, thereby enhancing the SCNRs of the slow and weak targets. This is in contrast to methods that rely solely on the magnitude of residuals [37], [40]. Furthermore, the theoretical statistics of the proposed detector are derived using a product clutter model with Gaussian noise, and then, a CFAR detection framework is established. Through simulations and real-data experiments, the superiority of the proposed method is validated by comparing it with mainstream techniques for detecting dim targets. Additionally, the computational complexity and detection sensitivity in relation to clutter heterogeneity, correlation coefficients between pairs of clutter-suppression residuals, and target parameters are analyzed, providing practical guidance for applications.

Notations: $*$, $(\cdot)^{\mathsf{T}}$, and $(\cdot)^{\mathsf{H}}$ are the conjugate, transpose and conjugate transpose, respectively. $|\cdot|$ denotes the modulus of a complex number, and $E[\cdot]$ denotes the mathematical expectation. $\mathbf{I}$ is the identity matrix of appropriate size, and i is the imaginary unit with $\mathrm{i}^2=-1$.

II. Radar Signal Model

Consider an airborne SAR system using a linear antenna array with M phase centers uniformly spaced by distance d along the aircraft's track direction, operating in a side-looking mode. The geometric configuration between the SAR and a ground moving target is shown in Fig. 1. During a coherent processing interval, the aircraft maintains a constant velocity v_{p} along its track direction at the height h. For the ground moving target, its azimuth and incident angles are expressed as α and θ, respectively, and the radial velocity along the radar's line-of-sight direction is denoted by v_{r}. The GMTI radar transmits electromagnetic waves through the M channels and uses identical signal processing chains to process the echo data sampled from each airborne radar array element. Following this process, a ground moving target is assumed to be properly match-filtered over the radar's signal bandwidth and coherently integrated, resulting in M range-Doppler maps in the case of range-Doppler processing or SAR imaging in the range and cross-range domains [41]. The

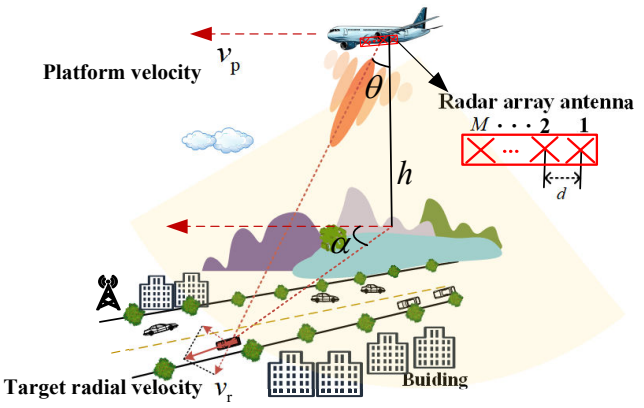

Fig. 1. Observation geometry illustrating relationship between the M-channel SAR system and ground moving targets in the side-looking GMTI mode.

along-track and cross-track directions are represented as the azimuth and slant range in each range-Doppler or SAR image, respectively. Subsequently, the spatial position alignment and the elimination of the constant amplitude and phase differences across the M SAR images are achieved through registration and calibration processing, as outline in [27].

For a pixel $k \in \{1, 2, \cdots, K\}$, let $\mathbf{z}(k) = [z_1(k), z_2(k), \cdots, z_M(k)]^{\mathsf{T}}$ represent a snapshot of the $M \times 1$ data vector from the processed M SAR images. Here, $z_m(k)$ denotes the complex signal in the m-th SAR image obtained from the m-th channel, $m \in \{1, 2, \cdots, M\}$. Accordingly, the binary hypothesis test for detecting target signals can be defined as

$$\begin{aligned} \mathrm{H}_0 &: \mathbf{z}(k) = \mathbf{c}(k) + \mathbf{n}(k), \\ \mathrm{H}_1 &: \mathbf{z}(k) = \mathbf{s}(k) + \mathbf{c}(k) + \mathbf{n}(k), \end{aligned} \tag{1}$$

where H_0 is the target-absent hypothesis, and H_1 is the target-present hypothesis; $\mathbf{c}(k)$ and $\mathbf{s}(k)$ are the clutter vector and the signal vector of a deterministic moving target, respectively; the noise vector $\mathbf{n}(k)$ follows a zero-mean complex Gaussian distribution, denoted as $\mathbf{n}(k) \sim \mathcal{CN}(\mathbf{0}, \sigma_{\mathrm{n}}^2\mathbf{I})$ with σ_{n}^2 being the noise power.

Under hypothesis H_1, the amplitudes of the focused target signal across all channels are assumed to be identical, such that $\mathbf{s}(k)$ can be expressed as

$$\mathbf{s}(k) = x_{\mathrm{t}}(k)\mathbf{a}_{\mathrm{t}}(k), \tag{2}$$

where $x_{\mathrm{t}}(k)$ denotes the complex target amplitude, and $\mathbf{a}_{\mathrm{t}}(k)$ denotes the target spatial steering vector. For a ground moving target with radial velocity $v_{\mathrm{r}}(k)$, as shown in Fig. 1, the target Doppler $f_{\mathrm{t}}(k) = 2v_{\mathrm{r}}(k)/\lambda$ induces a phase shift of $2\pi f_{\mathrm{t}}(k)\frac{d/2}{v_{\mathrm{p}}}$ as the array traverses the effective baseline spacing $d/2$ [42], where λ is the radar wavelength. Then, $\mathbf{a}_{\mathrm{t}}(k)$ is given by

$$\mathbf{a}_{\mathrm{t}}(k) = \left[1, \exp\left(\mathrm{i}2\pi\frac{f_{\mathrm{t}}(k)d}{2v_{\mathrm{p}}}\right), \cdots, \exp\left(\mathrm{i}2\pi\frac{f_{\mathrm{t}}(k)(M-1)d}{2v_{\mathrm{p}}}\right)\right]^{\mathsf{T}}. \tag{3}$$

For the ground clutter from the environment, its statistical properties are often non-uniform due to the composite scattering features such as buildings, trees, and roads. In SAR images, the amplitude of clutter according to backscatter characteristics is commonly modeled using the product model [35]–[38], as follows

$$\mathbf{c}(k) = \Delta(k) \times x_0(k)\mathbf{a}_{\mathrm{c}}(k), \tag{4}$$

where $\Delta(k) \in [0, \infty)$ is the texture variable and describes the amplitude variation of ground backscatter; $x_0(k) \sim \mathcal{CN}(0, \sigma_{\mathrm{c}}^2)$ denotes the complex Gaussian-distributed amplitude, with zero mean and an average power σ_{c}^2, while $\mathbf{a}_{\mathrm{c}}(k)$ is the spatial steering vector associated with clutter as

$$\mathbf{a}_{\mathrm{c}}(k) = \left[1, \exp\left(\mathrm{i}2\pi\frac{f_{\mathrm{c}}(k)d}{2v_{\mathrm{p}}}\right), \cdots, \exp\left(\mathrm{i}2\pi\frac{f_{\mathrm{c}}(k)(M-1)d}{2v_{\mathrm{p}}}\right)\right]^{\mathsf{T}}, \tag{5}$$

where $f_{\mathrm{c}}(k) = 2v_{\mathrm{c}}(k)/\lambda$ is the clutter Doppler frequency, and $v_{\mathrm{c}}(k)$ denotes the radial velocity of ground clutter. In particular, we have $\mathbf{a}_{\mathrm{c}}(k) \approx [1, \cdots, 1]^{\mathsf{T}}$, as $v_{\mathrm{c}}(k) \approx 0$ m/s.

To detect moving targets in a clutter-plus-noise environment, it is essential to reject the clutter in SAR images. Without loss of generality, under the adaptive matched filtering framework that optimally combines the array outputs in the range-Doppler or SAR images using an $M \times 1$ optimal weight vector $\mathbf{u}(k)$ [43], the clutter suppression result is given by

$$y(k) = \mathbf{u}^{\mathsf{H}}(k)\mathbf{z}(k), \tag{6}$$

where $\mathbf{u}(k) = \dfrac{\mathbf{R}^{-1}(k)\mathbf{a}_{\mathrm{t}}(k)}{\mathbf{a}_{\mathrm{t}}^{\mathsf{H}}(k)\mathbf{R}^{-1}(k)\mathbf{a}_{\mathrm{t}}(k)}$ is the optimal filter weight, $\mathbf{R}(k)$ is the CCM which can be estimated from Q i.i.d. samples selected in the vicinity of pixel k as $\hat{\mathbf{R}}(k) = \frac{1}{Q}\sum_{q=1}^{Q}\tilde{\mathbf{z}}_k(q)\tilde{\mathbf{z}}_k^{\mathsf{H}}(q)$ [44], and $\tilde{\mathbf{z}}_k(q) = [z_1(q), z_2(q), \cdots, z_M(q)]^{\mathsf{T}}$ denotes the snapshot of pixel k with the i.i.d. sample q, being the $M \times 1$ data vector. The magnitude test based on the residual amplitude is then formulated as [37], [38]

$$\beta(k) = \frac{|y(k)|^2}{\sigma_{\mathrm{cn}}^2} \underset{\mathrm{H}_0}{\overset{\mathrm{H}_1}{\gtrless}} \eta_0 \tag{7}$$

where σ_{cn}^2 represents the average power of clutter residuals, and η_0 is the detection threshold. H_1 is declared when β exceeds η_0, and otherwise, H_0 is declared.

III. Proposed Method

In this section, we propose a target detector by combining the magnitude and phase information in multichannel clutter suppression. The functional block diagram of this method is shown in Fig. 2. In brief, the magnitude-based test β based on the clutter suppression residuals with the M-channel SAR images and the phase factor ϕ exploiting the interferometric phase φ estimated over two clutter suppression residuals from the previous and subsequent $M-1$ SAR images, respectively, are firstly constructed. Then, the proposed target detection metric γ is formulated as the product of β and ϕ, and its statistics under the hypothesis H_0 are estimated using the clutter samples. Finally, the target detection threshold η under a given Pfa (P_{f}) is determined, and potential targets are decided. In what follows, the details of the proposed method are introduced.

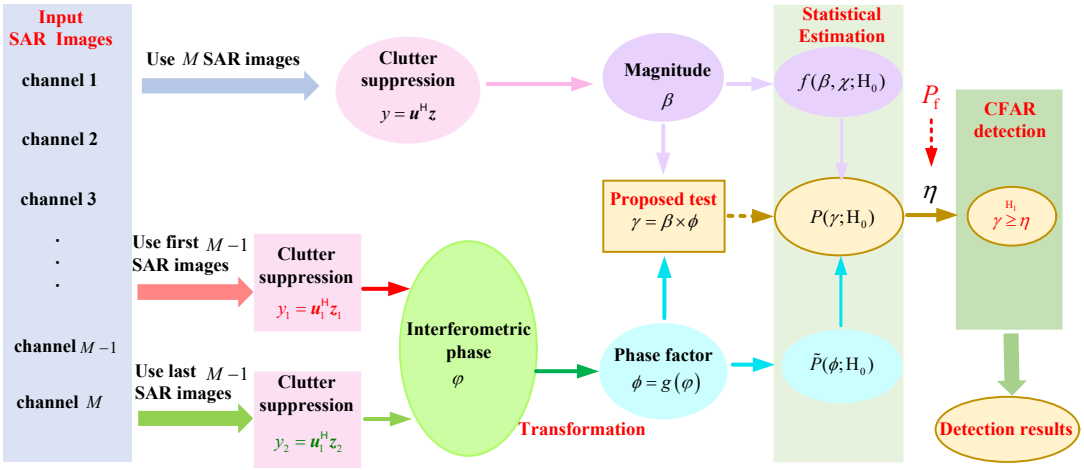

Fig. 2. Functional block diagram of the proposed method.

A. Target Detector

Initially, the SAR images from the first and last $M-1$ channels are used to construct two data vectors for a given pixel k as follows

$$\mathbf{z}_1(k) = [z_1(k), z_2(k), \cdots, z_{M-1}(k)]^{\mathsf{T}}, \tag{8a}$$

$$\mathbf{z}_2(k) = [z_2(k), z_3(k), \cdots, z_M(k)]^{\mathsf{T}}. \tag{8b}$$

Note that $\mathbf{z}_1(k)$ and $\mathbf{z}_2(k)$ differ by a time delay of $d/(2v_{\mathrm{p}})$ due to the platform's along-track velocity (v_{p}) across the channel spacing d. Nevertheless, this time delay does not impact the spatial steering vector, allowing the same filtering processor $\mathbf{u}_1(k)$ to be applied to both data vectors for clutter rejection. This process yields

$$y_1(k) = \mathbf{u}_1^{\mathsf{H}}(k)\mathbf{z}_1(k), \tag{9a}$$

$$y_2(k) = \mathbf{u}_1^{\mathsf{H}}(k)\mathbf{z}_2(k), \tag{9b}$$

where $\mathbf{u}_1(k)$ can be formulated using the following optimal adaptive matched filter:

$$\mathbf{u}_1(k) = \frac{\mathbf{R}_1^{-1}(k)\mathbf{a}_{\mathrm{t1}}(k)}{\mathbf{a}_{\mathrm{t1}}^{\mathsf{H}}(k)\mathbf{R}_1^{-1}(k)\mathbf{a}_{\mathrm{t1}}(k)}, \tag{10a}$$

$$\hat{\mathbf{R}}_1(k) = \frac{1}{Q}\sum_{q=1}^{Q}\tilde{\mathbf{z}}_{1,k}(q)\tilde{\mathbf{z}}_{1,k}^{\mathsf{H}}(q), \tag{10b}$$

$$\mathbf{a}_{\mathrm{t1}}(k) = \left[1, \cdots, \exp\left(\mathrm{i}2\pi f_{\mathrm{t}}(k)\frac{(M-1)d}{2v_{\mathrm{p}}}\right)\right]^{\mathsf{T}}, \tag{10c}$$

where $\hat{\mathbf{R}}_1(k)$ is the estimation of CCM with sample data from the first $M-1$ channels, and $\tilde{\mathbf{z}}_{1,k}(q) = [z_1(q), z_2(q), \cdots, z_{M-1}(q)]^{\mathsf{T}}$ denotes the snapshot of pixel k with the i.i.d. sample q, being the $(M-1)\times 1$ data vector, while $\mathbf{a}_{\mathrm{t1}}(k)$ is the target spatial steering vector across the $M-1$ channels. During the clutter suppression processing, the Doppler frequency $f_{\mathrm{t}}(k)$ (in (10c)) of the moving target is usually unknown before target detection. To reduce the output power for potential targets, a group of candidates $f_{\mathrm{t1}}, f_{\mathrm{t2}}, \cdots$ are used to search for an optimal one that can output a maximum SCNR, as detailed by the image-domain optimized STAP method [2].

Following the signal model in (1), we have $\mathbf{z}_1(k) = \mathbf{c}_1(k) + \mathbf{n}_1(k)$ and $\mathbf{z}_2(k) = \mathbf{c}_2(k) + \mathbf{n}_2(k)$ under the hypothesis H_0, while $\mathbf{z}_1(k) = \mathbf{s}_1(k) + \mathbf{c}_1(k) + \mathbf{n}_1(k)$ and $\mathbf{z}_2(k) = \mathbf{s}_2(k) + \mathbf{c}_2(k) + \mathbf{n}_2(k)$ under the hypothesis H_1. Here, $\mathbf{s}_1$, $\mathbf{c}_1$, and $\mathbf{n}_1$ denote the target, clutter and noise signals in $\mathbf{z}_1$, respectively, while $\mathbf{s}_2$, $\mathbf{c}_2$, and $\mathbf{n}_2$ correspond to the target, clutter and noise signals in $\mathbf{z}_2$, respectively. Assuming identical channel responses and no additional errors such as channel location uncertainties, the time delay $d/(2v_{\mathrm{p}})$ introduces a phase difference related to the scatter's Doppler frequency between $\mathbf{z}_1(k)$ and $\mathbf{z}_2(k)$, expressed as

$$\mathbf{c}_2(k) = \mathbf{c}_1(k)\exp\left(\mathrm{i}2\pi f_{\mathrm{c}}(k)\frac{d}{2v_{\mathrm{p}}}\right), \tag{11a}$$

$$\mathbf{s}_2(k) = \mathbf{s}_1(k)\exp\left(\mathrm{i}2\pi f_{\mathrm{t}}(k)\frac{d}{2v_{\mathrm{p}}}\right). \tag{11b}$$

Accordingly, the residual signals $y_1(k)$ and $y_2(k)$ in (9) can be reformulated under the hypothesis H_0 as follows

$$\mathrm{H}_0: \quad y_1(k) = y_{\mathrm{c1}}(k) + y_{\mathrm{n1}}(k), \tag{12a}$$

$$y_2(k) = y_{\mathrm{c1}}(k)\exp\left(\mathrm{i}2\pi f_{\mathrm{c}}(k)\frac{d}{2v_{\mathrm{p}}}\right) + y_{\mathrm{n2}}(k), \tag{12b}$$

whereas, under the hypothesis H_1, they are expressed as

$$\mathrm{H}_1: \quad y_1(k) = y_{\mathrm{s1}}(k) + y_{\mathrm{c1}}(k) + y_{\mathrm{n1}}(k), \tag{13a}$$

$$y_2(k) = y_{\mathrm{s1}}(k)\exp\left(\mathrm{i}2\pi f_{\mathrm{t}}(k)\frac{d}{2v_{\mathrm{p}}}\right) + y_{\mathrm{c1}}(k)\exp\left(\mathrm{i}2\pi f_{\mathrm{c}}(k)\frac{d}{2v_{\mathrm{p}}}\right) + y_{\mathrm{n2}}(k), \tag{13b}$$

where $y_{\mathrm{c1}}(k) = \mathbf{u}_1^{\mathsf{H}}(k)\mathbf{c}_1(k)$ and $y_{\mathrm{s1}}(k) = \mathbf{u}_1^{\mathsf{H}}(k)\mathbf{s}_1(k)$ denote the residuals associated with the clutter and target signals, respectively; $y_{\mathrm{n1}}(k) = \mathbf{u}_1^{\mathsf{H}}(k)\mathbf{n}_1(k)$ and $y_{\mathrm{n2}}(k) = \mathbf{u}_1^{\mathsf{H}}(k)\mathbf{n}_2(k)$ denote the residuals of the noise signals in $\mathbf{z}_1(k)$ and $\mathbf{z}_2(k)$, respectively, with $|y_{\mathrm{n1}}(k)| \approx |y_{\mathrm{n2}}(k)|$.

Applying the complex interferometry over $y_1(k)$ and $y_2(k)$, we extract the interferometric phase by

$$\varphi(k) = \arg\left[y_1(k)y_2^*(k)\right], \tag{14}$$

where $\arg[\cdot]$ denotes the phase of a complex, ranging in $[-\pi, \pi]$.

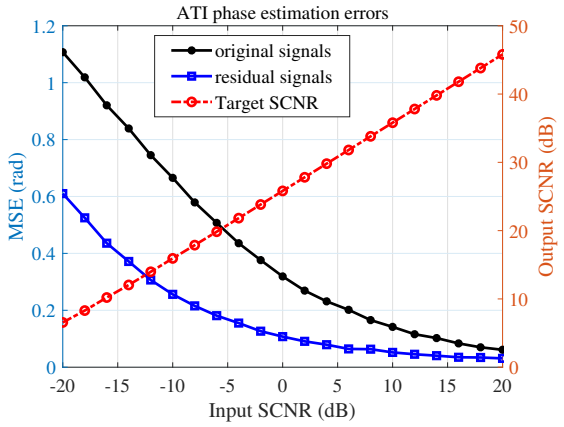

Fig. 3. MSE of ATI phase estimation versus input SCNRs for $v_{\mathrm{r}} = 2$ m/s.

Under the hypothesis H_0, assume that a large stationary clutter residual signal present, where $|y_{\mathrm{c1}}| \gg |y_{\mathrm{n1}}| \approx |y_{\mathrm{n2}}|$ in (12), and thus, the interferometric phase $\varphi(k)$ through (14) approximates 0. If the residuals are like noise signals after the clutter suppression processing, i.e., $|y_{\mathrm{c1}}| \approx |y_{\mathrm{n1}}| \approx |y_{\mathrm{n2}}|$ in (12), the interferometric phase $\varphi(k)$ reflects the phase difference between two channels for the noise signal, and usually distributes in $[-\pi, \pi]$.

On the flip side, when a moving target signal is present alongside clutter and noise signals in the pixel, the clutter signal is nearly completely rejected and the residual of the moving target signal typically exhibits a relatively large magnitude. In this case, in (13), we have

$$|y_{\mathrm{s1}}(k)| = |\mathbf{u}_1^{\mathsf{H}}(k)\mathbf{s}_1(k)| \gg |y_{\mathrm{c1}}(k)| > |y_{\mathrm{n1}}(k)|. \tag{15}$$

After applying (14) across the residual signals $y_1(k)$ and $y_2(k)$, one has $\varphi(k) \approx 2\pi f_{\mathrm{t}}(k)\frac{d}{2v_{\mathrm{p}}}$. Assume that the moving target has a radial velocity $v_{\mathrm{r}}(k)$, such that $f_{\mathrm{t}}(k) = \frac{2v_{\mathrm{r}}(k)}{\lambda}$. Then, the radial velocity of the moving target can be estimated using the interferometric phase $\varphi(k)$ as

$$\tilde{v}_{\mathrm{r}}(k) = \frac{\lambda v_{\mathrm{p}}}{2\pi d}\varphi(k). \tag{16}$$

The unambiguous velocity estimation by (16) ranges from $[-\lambda v_{\mathrm{p}}/(2d), \lambda v_{\mathrm{p}}/(2d)]$. If $|v_{\mathrm{r}}(k)| > \lambda v_{\mathrm{p}}/(2d)$, an ambiguity velocity with a period of $\lambda v_{\mathrm{p}}/d$ will appear in the estimation [42]. Compared with the classical ATI phase over the dual-channel original signals $z_1(k)$ and $z_2(k)$ in (8a) [31], [45], [46], this ATI phase estimated from two residual signals $y_1(k)$ and $y_2(k)$ in (9) reduces the clutter interference by suppressing clutter, and thus, can improve the ATI phase estimation accuracy for the targets with low SCNRs. We conduct a simulation comparison between the estimation of target ATI phases across dual-channel original signals and two residual signals. In the simulation, the real-world clutter data (refer to the description in Section IV-B) are used, and the targets are simulated based on the signal models in (2) and (3). The estimation results of target ATI phases and the mean square errors (MSE) are counted, respectively, and the results for $v_{\mathrm{r}} = 2$ m/s are shown in Fig. 3. The output SCNRs of the simulated targets in the clutter suppression processing are shown by the right vertical axis. The less MSE for the ATI phases from residual signals indicate more accuracy in target radial velocity estimation, and the estimation improvements are especially significant for the targets with lower input SCNRs.

In the analysis of $\varphi(k)$ outlined above, a notable difference emerges between large clutter residuals and moving targets. Under the hypothesis H_0, suppose that a large residual signal is present, which may cause false alarms when applying the magnitude-based detection via (7). However, $\varphi(k) \approx 0$, as indicated by (12) and (14). As to the hypothesis H_1, the estimation of $\varphi(k)$ using (14) is approximately proportional to the target's radial velocity $v_{\mathrm{r}}(k)$ according to (15) and (16). Thus, moving targets can be effectively distinguished from large clutter residuals based on the value of $\varphi(k)$.

Next, based on the estimation result $\tilde{v}_{\mathrm{r}}(k)$ and the spatial structure across the two adjusted channels, the corresponding steering vector for the residual can be constructed as

$$\mathbf{b}(k) = \left[1, \exp\left(\mathrm{i}2\pi\frac{\tilde{v}_{\mathrm{r}}(k)d}{\lambda v_{\mathrm{p}}}\right)\right]^{\mathsf{T}} = \left[1, \exp\left(\mathrm{i}\varphi(k)\right)\right]^{\mathsf{T}}. \tag{17}$$

For large clutter residuals, the steering vector in (17) can be approximated as $\mathbf{b}_0 = [1, 1]^{\mathsf{T}}$, since $\tilde{v}_{\mathrm{r}}(k) \approx 0$ m/s. Based on this, we proceed to estimate the subspace similarity between the residual and $\mathbf{b}_0$ as

$$\epsilon(k) = \frac{|\mathbf{b}^{\mathsf{H}}(k)\mathbf{b}_0|}{\sqrt{|\mathbf{b}^{\mathsf{H}}(k)\mathbf{b}(k)||\mathbf{b}_0^{\mathsf{H}}\mathbf{b}_0|}}, \tag{18}$$

where $\epsilon(k) \in [0, 1]$ and is a function of the interferometric phase $\varphi(k)$. A lager $\epsilon(k)$ indicates a greater similarity between the residual and clutter.

By multiplying a phase-based factor $1 - \epsilon(k)$ with the magnitude test $\beta(k)$ that outputs from the M-channel clutter suppression (see (7)), we obtain $\gamma(k) = \beta(k) \times (1 - \epsilon(k))$, which further helps in rejecting the strong and isolated clutter residuals. The phase factor $1 - \epsilon(k)$ is a function of $\varphi(k)$, expressed as

$$\phi(k) = g\left(\varphi(k)\right) = 1 - \epsilon(k). \tag{19}$$

As such, the novel target detector is formulated as

$$\gamma(k) = \beta(k) \times \phi(k) \underset{\mathrm{H}_0}{\overset{\mathrm{H}_1}{\gtrless}} \eta \tag{20}$$

where the hypothesis H_1 is declared when $\gamma(k)$ exceeds the detection threshold η, and otherwise, the hypothesis H_0 is declared.

Following the CFAR detection rule [47], under the clutter-plus-noise background, the statistics of the proposed test γ should be estimated, so that the detection threshold η can be determined with a constant Pfa regardless of changes in the environment. In what follows, the statistical estimation under the two hypotheses is detailed in subsection III-B, and the CFAR detection process is summarized in subsection III-C.

B. Statistical Estimation

In complex environments, clutter data typically consists of a mixture of backscatter types with varying reflectivity. As described by the product model in (4), the texture variable Δ can vary across pixels in SAR images, representing the

backscatter changes in heterogeneous clutter backgrounds. Various statistical models have been developed for Δ in recent years [35]–[38]. For urban areas, which are critically discussed herein, the inverse chi-square function has been extensively used for SAR-GMTI applications [35], [37], and the probability distribution function (pdf) of Δ is given by

$$f_{\Delta}(\delta) = \frac{2\left(\chi-1\right)^{\chi}}{\Gamma(\chi)}\delta^{-(2\chi+1)}\exp\left(-\frac{\chi-1}{\delta^2}\right), \tag{21}$$

where $\Gamma(\cdot)$ denotes the Gamma function, and the degree of heterogeneity for the clutter background is reflected by the texture parameter χ. A smaller value of χ indicates a more heterogeneous clutter background.

Using this model to characterize heterogeneous clutter backgrounds, we now revisit the statistics of the proposed test γ. From (20), γ is formulated as the product of the magnitude test β and a phase test ϕ. According to the theoretical derivations in [37], [48] for the single-look case, the pdf of β under the hypothesis H_0 is given by

$$f(\beta,\chi;\mathrm{H}_0) = \frac{\chi\left(\chi-1\right)^{\chi}}{\left(\chi-1+\beta\right)^{1+\chi}} \tag{22}$$

where the texture parameter χ can be evaluated using $\chi = 1+\frac{m_2}{m_2-2}$ with $m_2 = \mathrm{E}[|\beta|^2]$ being the second moment over clutter samples, and $\chi > 2$ according to the nonnegativity of the pdf. In practice, this estimator may be inaccurate, and χ can be estimated to achieve the required fit accuracy. For a deterministic moving target, assume that its maximum likelihood estimate of the magnitude test is ω, and the pdf for the hypothesis H_1 is formulated as

$$\begin{aligned} f(\beta,\chi,\omega;\mathrm{H}_1) = &\frac{\chi(\chi-1)^{\chi}}{\left(\omega+\chi-1+\beta\right)^{1+\chi}} \\ &\times {}_2F_1\left(\frac{\chi+1}{2},\frac{\chi+2}{2};1;\frac{4\omega\beta}{\left(\omega+\chi-1+\beta\right)^2}\right), \end{aligned} \tag{23}$$

where ${}_2F_1(\cdot)$ denotes the Gaussian hypergeometric function.

On the other hand, ϕ is a function of the interferometric phase φ, and thus, the pdf of ϕ can be derived from the pdf of φ. Based on the derivations in [35], [38], [45], [46], the pdf of φ under the hypothesis H_0 is given by

$$\begin{aligned} f_{\mathrm{p}}(\varphi,\rho,\varphi_{\mathrm{c}};\mathrm{H}_0) = &\frac{\Gamma(3/2)(1-\rho^2)\rho\cos(\varphi-\varphi_{\mathrm{c}})}{2\sqrt{\pi}(1-\rho^2\cos^2(\varphi-\varphi_{\mathrm{c}}))^{3/2}} \\ &+\frac{(1-\rho^2)}{2\pi}{}_2F_1\left(1,1;1/2;\rho^2\cos^2\left(\varphi-\varphi_{\mathrm{c}}\right)\right), \end{aligned} \tag{24}$$

where φ_{c} denotes the interferometric phase estimate for the clutter residual, which is equal to π [38]; ρ represents the correlation coefficient between y_1 and y_2, which can be estimated across all residual samples as

$$\rho = \frac{|E[y_1 y_2^*]|}{\sqrt{E[|y_1|^2]E[|y_2|^2]}}, \tag{25}$$

where $0 \le \rho \le 1$.

When the target parameters φ_{t} and ρ_{t} are known or estimated using target samples. The pdf of φ under the hypothesis H_1 is

$$\begin{aligned} f_{\mathrm{p}}(\varphi,\rho_{\mathrm{t}},\varphi_{\mathrm{t}};\mathrm{H}_1) = &\frac{\Gamma(3/2)(1-{\rho_{\mathrm{t}}}^2)\rho_{\mathrm{t}}\cos(\varphi-\varphi_{\mathrm{t}})}{2\sqrt{\pi}(1-{\rho_{\mathrm{t}}}^2\cos^2(\varphi-\varphi_{\mathrm{t}}))^{3/2}} \\ &+\frac{(1-{\rho_{\mathrm{t}}}^2)}{2\pi}{}_2F_1(1,1;1/2;{\rho_{\mathrm{t}}}^2\cos^2(\varphi-\varphi_{\mathrm{t}})). \end{aligned} \tag{26}$$

Unfortunately, given the pdfs of φ defined by the above functions and the mapping relationship $\phi = g(\varphi)$ from (17), (18), and (19), it is intractable to analytically derive the pdf of ϕ. Towards this end, a numerical approximation approach is adopted. First, the interferometric phase φ is discretized over the range from $-\pi$ to π using a step size of φ_0, i.e., $\varphi_1 = -\pi, \varphi_2 = -\pi+\varphi_0, \varphi_3 = -\pi+2\varphi_0, \cdots, \varphi_L = \pi$, where the size φ_0 is chosen to be extremely small to ensure calculation accuracy, such as $\varphi_0 = \pi/1000$. The distribution probability with respect to the discretized variable $\varphi_l, l = 1,2,\cdots,L$, is computed by

$$\tilde{P}(\varphi_l;\mathrm{H}_0) = \frac{f_{\mathrm{p}}(\varphi_l,\rho,\varphi_{\mathrm{c}};\mathrm{H}_0)}{\sum_{p=1}^{p=L} f_{\mathrm{p}}(\varphi_p,\rho,\varphi_{\mathrm{c}};\mathrm{H}_0)}, \tag{27a}$$

$$\tilde{P}(\varphi_l;\mathrm{H}_1) = \frac{f_{\mathrm{p}}(\varphi_l,\rho_{\mathrm{t}},\varphi_{\mathrm{t}};\mathrm{H}_1)}{\sum_{p=1}^{p=L} f_{\mathrm{p}}(\varphi_p,\rho_{\mathrm{t}},\varphi_{\mathrm{t}};\mathrm{H}_1)}. \tag{27b}$$

Then, $\phi_l = g(\varphi_l)$ is computed for each φ_l using (17), (18), and (19), resulting in the sequence $\phi_1,\phi_2,\cdots,\phi_L$. The distribution probabilities for the discretized variable $\phi \in \{\phi_1,\cdots,\phi_L\}$ under the two hypotheses H_0 and H_1 can be estimated as

$$P(\phi;\mathrm{H}_0) = \sum \tilde{P}(\varphi_l;\mathrm{H}_0) \tag{28a}$$

$$P(\phi;\mathrm{H}_1) = \sum \tilde{P}(\varphi_l;\mathrm{H}_1) \tag{28b}$$

$$\text{s.t.} \begin{cases} \varphi_l \in \{\varphi_1,\varphi_2,\cdots,\varphi_L\} \\ g(\varphi_l) = \phi_l \\ |\phi_l - \phi| \le \epsilon \end{cases}$$

where ϵ denotes the quantification error, which is set as the minimum and non-zero difference between any two discretized variables in $\{\phi_1,\phi_2,\cdots,\phi_L\}$.

The above pdfs of ϕ are further normalized as

$$\tilde{P}(\phi;\mathrm{H}_0) = \frac{P(\phi;\mathrm{H}_0)}{\sum_{\phi} P(\phi;\mathrm{H}_0)}, \tag{29a}$$

$$\tilde{P}(\phi;\mathrm{H}_1) = \frac{P(\phi;\mathrm{H}_1)}{\sum_{\phi} P(\phi;\mathrm{H}_1)}, \tag{29b}$$

which ensures that $\sum_{\phi}\tilde{P}(\phi;\mathrm{H}_0) = 1$ and $\sum_{\phi}\tilde{P}(\phi;\mathrm{H}_1) = 1$ in the numerical calculation.

Subsequently, using the relationship $\gamma(k) = \beta(k)\times\phi(k)$ defined in (20) and assuming the statistical independence between between β and ϕ, the pdfs for γ under the two hypotheses can be approximated as

$$P(\gamma;\mathrm{H}_0) \approx \sum_{\phi} \tilde{P}(\phi;\mathrm{H}_0) f_{\mathrm{T}_1}(\frac{\gamma}{\phi},\chi;\mathrm{H}_0), \tag{30a}$$

$$P(\gamma;\mathrm{H}_1) \approx \sum_{\phi} \tilde{P}(\phi;\mathrm{H}_1) f_{\mathrm{T}_1}(\frac{\gamma}{\phi},\chi,\omega;\mathrm{H}_1). \tag{30b}$$

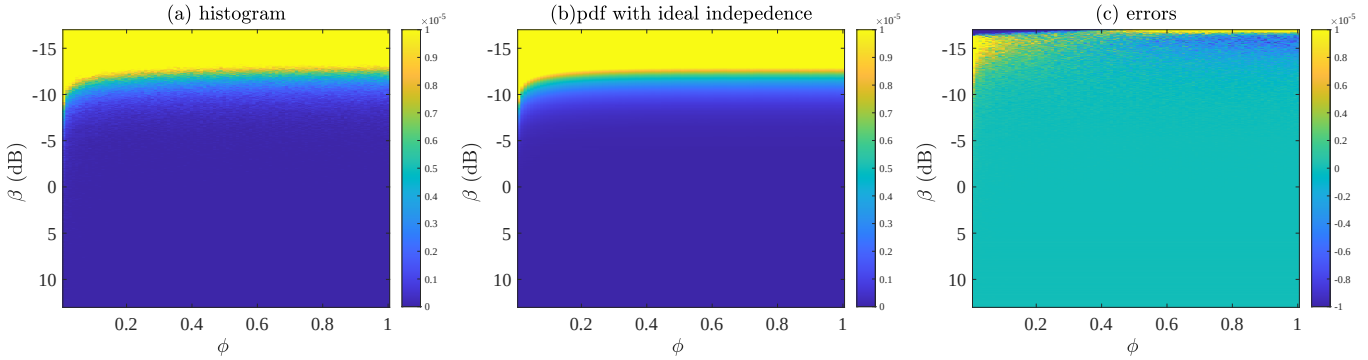

Fig. 4. Joint distribution characteristics of β and ϕ in homogeneous clutter background: (a) histogram, (b) theoretical pdf in (30a) with $\hat{\chi} = 162$, $\hat{\rho} = 0.15$, and $\hat{\varphi}_{\mathrm{c}} = \pi$, and (c) errors between the results in Fig. 4(a) and Fig. 4(b).

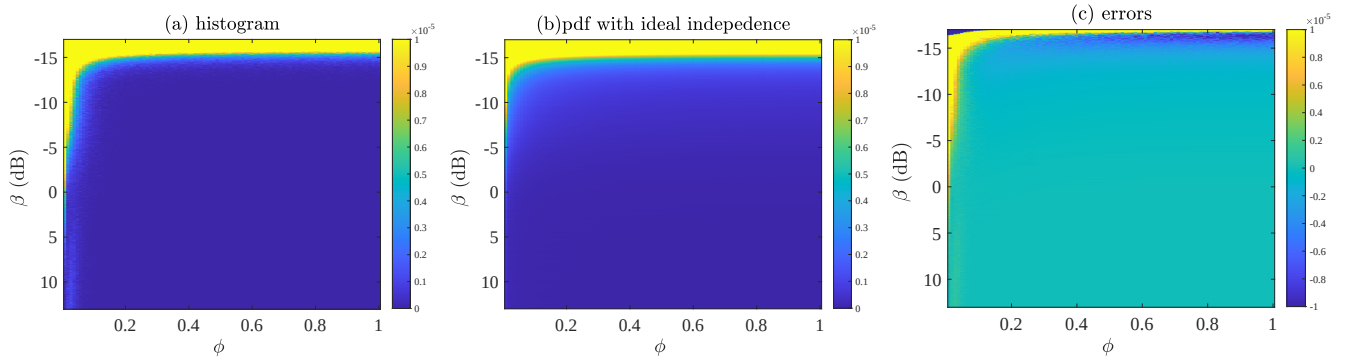

Fig. 5. Joint distribution characteristics of β and ϕ in heterogeneous clutter background: (a) histogram, (b) theoretical pdf in (30a) with $\hat{\chi} = 2.1$, $\hat{\rho} = 0.38$, and $\hat{\varphi}_{\mathrm{c}} = \pi$, and (c) errors between the results in Fig. 5(a) and Fig. 5(b).

Given a Pfa, i.e., P_{f}, in target detection, the threshold η in (20) can be determined by

$$P_{\mathrm{f}} = \int_{\eta}^{+\infty} P(\gamma; \mathrm{H}_0)\mathrm{d}\gamma = 1 - \int_{0}^{\eta} P(\gamma; \mathrm{H}_0)\mathrm{d}\gamma. \tag{31}$$

Under the detection threshold η, the corresponding Pd, i.e., P_{d}, is

$$P_{\mathrm{d}} = \int_{\eta}^{+\infty} P(\gamma; \mathrm{H}_1)\mathrm{d}\gamma = 1 - \int_{0}^{\eta} P(\gamma; \mathrm{H}_1)\mathrm{d}\gamma. \tag{32}$$

The derivation of the proposed test statistics in (30) relies on the assumption of statistical independence between the magnitude test β and phase factor ϕ. Theoretically, β and ϕ are not strictly independent in statistics, and appear to be correlated for clutter and target residuals. Nevertheless, through the following Monte Carlo simulations, it is found that the correlation between β and ϕ has only little influence on statistics of γ and (30) can work with acceptable accuracy.

In the simulation of the hypothesis H_0, the homogeneous clutter background (a constant CNR of 10 dB) and heterogeneous clutter background (CNRs varying from 15 dB to 50 dB) are created, and more details on the process can refer to Section IV-A. The joint distribution characteristics of β and ϕ in the homogeneous clutter background are shown in Fig. 4, where Fig. 4(a) is the histogram of the data, Fig. 4(b) is theoretical pdf in (30a) with estimated parameters $\hat{\chi} = 162$, $\hat{\rho} = 0.15$, and $\hat{\varphi}_{\mathrm{c}} = \pi$, and Fig. 4(c) is the difference between Fig. 4(a) and Fig. 4(b). The results in the heterogeneous clutter background are shown in Fig. 5, where the theoretical pdf in (30a) is obtained with estimated parameters $\hat{\chi} = 2.1$, $\hat{\rho} = 0.38$, and $\hat{\varphi}_{\mathrm{c}} = \pi$. In Fig. 4(c) and Fig. 5(c), the differences between the histogram and theoretical pdf mostly occur near $\beta \approx 0$ and $\phi \approx 0$, and include both positive and negative deviations. These differences are more significant in heterogeneous clutter background, which implies the existing corelation between β and ϕ for clutter residuals. Nevertheless, in the proposed test $\gamma = \beta \times \phi$, the products of β and ϕ at $\beta \approx 0$ and $\phi \approx 0$ approximate zero, and these positive and negative deviations may be partially canceled at $\gamma \approx 0$ with (30a). The statistical estimation comparisons for γ in the homogeneous and heterogeneous clutter backgrounds are shown in Figs. 6(a) and (b), respectively, where for a given Pfa, the target detection thresholds η are calculated using (30a) (marked with'ideal independence') and estimated via Monte Carlo simulation(marked with 'estimated'), respectively. In the homogeneous background, (30a) can accurately predict the CFAR statistics. For the heterogeneous background, small deviations for η have occurred due to the correlation effects in clutter residuals. Furthermore, the corresponding ROC curves for targets with the input SNR of 25 dB and radial velocities of 2 m/s and 4 m/s in the heterogeneous clutter background are depicted in Fig. 6(c). Specifically, under the given Pfa, the Pd is determined by counting the number of target cells exceeding the detection threshold. The results verify that the correlation effects on the proposed CFAR statistics can be ignored.

Under the hypothesis H_1, the target with an input SNR of 25 dB and a radial velocity of 2 m/s is simulated in the clutter background. The joint distribution characteristics of β and ϕ are shown in Fig. 7, where Fig. 7(a) is the histogram, Fig. 7(b) is theoretical pdf in (30b) with estimated parameters

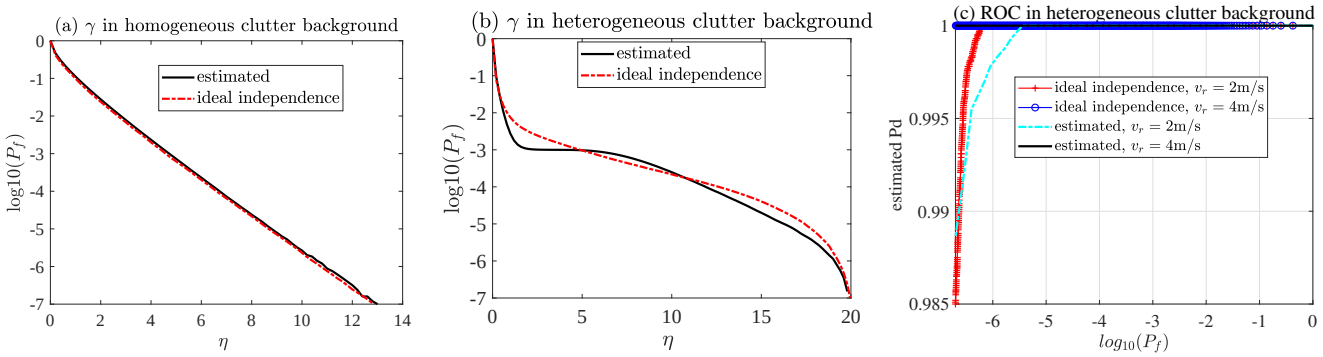

Fig. 6. Statistical estimation comparisons between (30a) (marked with'ideal independence') and Monte Carlo simulation (marked with 'estimated') for the proposed test γ: (a) and (b) are the detection threshold η versus Pfas for homogeneous and heterogeneous clutter backgrounds, respectively, and (c) is the ROC in terms of the estimated Pd versus the Pfa in heterogeneous clutter background, with an input SNR of 25 dB, target radial velocities of 2 m/s and 4 m/s.

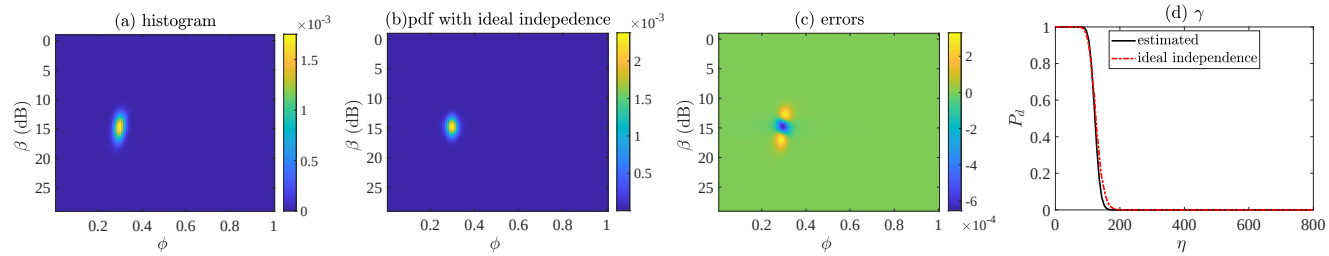

Fig. 7. Joint distribution characteristics of β and ϕ for the target with input SNR 25 dB and radial velocity 2 m/s: (a) histogram, (b) theoretical pdf in (30a) with $\hat{\omega} = 413, \hat{\chi} = 162$, $\hat{\rho} = 0.9878$, and $\hat{\varphi}_{\mathrm{t}} = 1.54$, and (c) errors between the results in Fig. 7(a) and Fig. 7(b). (d) Pd estimation comparisons between (30b) ('ideal independence') and Monte Carlo simulation ('estimated') for γ.

$\hat{\omega} = 413, \hat{\chi} = 162$, $\hat{\rho} = 0.9878$, and $\hat{\varphi}_{\mathrm{t}} = 1.54$, and Fig. 4(c) is the difference between Fig. 7(a) and Fig. 7(b). The result implies the existing correlation between β and ϕ for target residuals. However, this correlation effect on the derived statistics of γ ((30b)) is rather little in the following comparisons. Given the η, the Pd values are estimated using (30b) (marked with 'ideal independence') and counting the number of target cells exceeding the detection threshold via Monte Carlo simulation (marked with 'estimated'), respectively, and the comparison result is shown in Fig. 7 (d). The high-accuracy prediction results can validate the feasibility of the independence assumption in this work. For more accurate statistics, other modeling and estimation technologies [36], [49] remain an open topic in future work.

C. Summary of the Proposed CFAR Detection

Based on the above theoretical performance analysis of the proposed test, the main procedures for the CFAR detection are summarized as follows.

- First, the adaptive matched filter, as given by (6), is applied to the data vector $\mathbf{z}$ from the M-channel SAR images, and then, the magnitude-based test β is formulated according to (7).
- Meanwhile, adaptive matched filtering with the previous and subsequent $M-1$ SAR images, respectively, as shown in (9), outputs two residuals. Based on this, the interferometric phase is estimated using (14), and the phase test ϕ is constructed, as given by (19).
- Next, the proposed target detection metric γ is formulated as the product of the magnitude test β and the phase test ϕ, as expressed by (20).
- Afterwards, estimate the statistical property of γ through (22), (24), (25), (27a), (28a), (29a), and (30a) over the data samples, and determine the target detection threshold η under a given P_{f} via (31).
- Finally, potential moving targets are detected by comparing the test with η.

During the above procedures, let M, K, and L represent the channel number, the pixel number of a SAR image, and the discretized number of the interferometric phase φ in $[-\pi, \pi]$, respectively. The computational complexities for the adaptive clutter suppression with filters $\mathbf{u}$ and $\mathbf{u}_1$ are expressed as $\mathcal{O}(M^3)$ and $\mathcal{O}((M-1)^3)$, respectively. Meanwhile, the computational complexities for constructing and statistically estimating the proposed test are $\mathcal{O}(K)$ and $\mathcal{O}(L)$, respectively. Therefore, the computational complexity for the proposed detection process is $\mathcal{O}(M^3) + \mathcal{O}(K) + \mathcal{O}(L)$.

IV. Simulations and Real-Data Experiments

A. Simulation Results

Simulation data based on the signal models described in (2) to (5) are created to evaluate the target detection performance, and the radar parameters are listed in Tab. I. In the simulation, there are 700 heterogeneous clutter samples with varying CNRs ranging from 15 dB to 50 dB, randomly distributed in the clutter background. Additionally, there are 300 homogeneous clutter samples, each with a constant CNR of 10 dB. A moving target is simulated and added at the sample position 800. To account for inconsistent channel responses, a random channel phase error with zero mean and a variance of 0.5° is introduced. The above parameter settings are similar to the real-data conditions in Section IV-B, leading to the

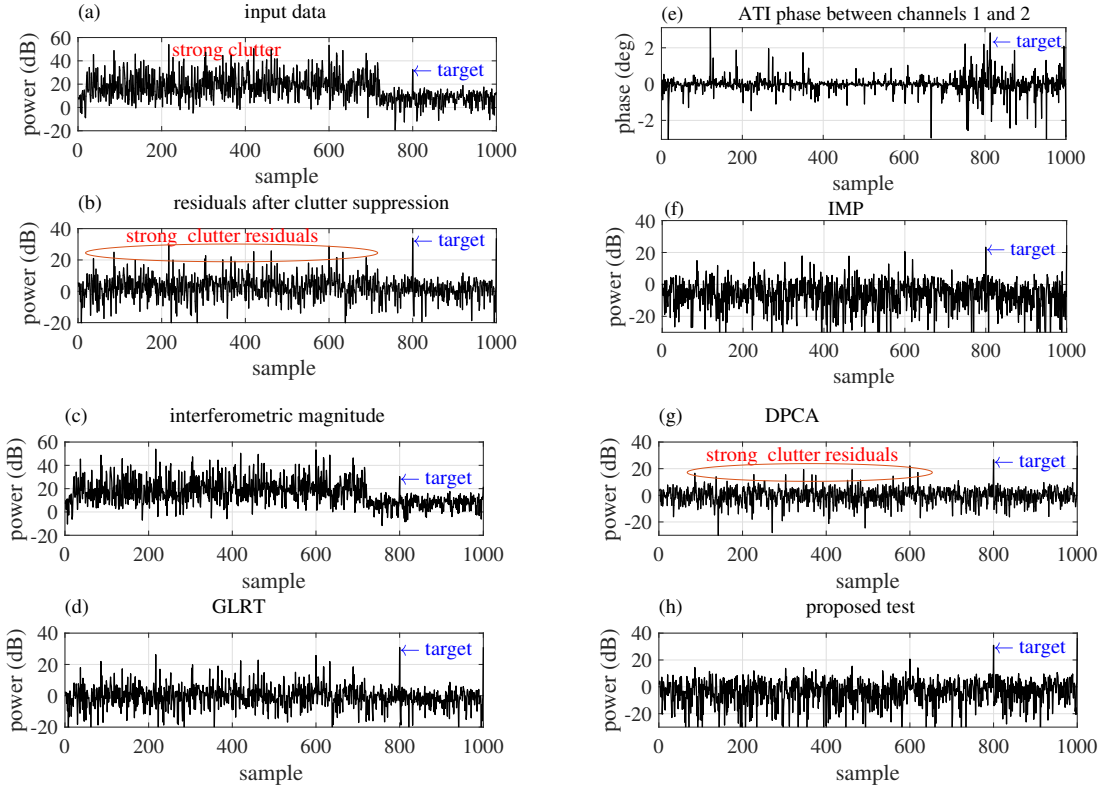

Fig. 8. Comparison of different detection methods with $M = 4$, $\hat{\chi} = 2.1$, $v_r = 2$ m/s, and an input SNR of 25 dB: (a) magnitude of SAR-image sample, (b) normalized magnitude of clutter-suppression residuals, (c) interferometric magnitude, (d) GLRT, (e) ATI phase between channels 1 and 2 , (f) IMP, (g) DPCA test, and (h) the proposed test, respectively.

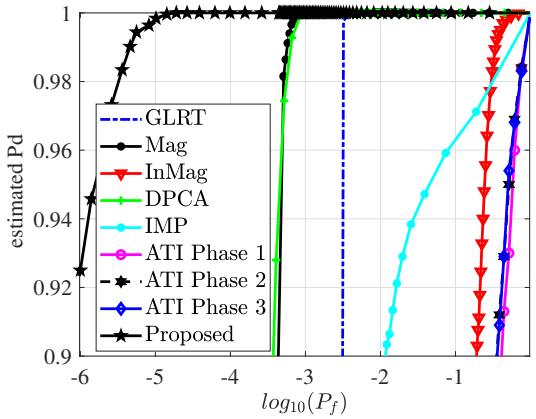

Fig. 9. P_d versus P_f for the single test with an input SNR of 25 dB and $v_r = 2$ m/s, where the ATI phase 1, ATI phase 2, and ATI phase 3 represent the interferometric phase between channels 1 and 2, the interferometric phase between channels 1 and 3, and the interferometric phase between channels 1 and 4, respectively.

average dual-channel correlation coefficient about 0.9965 and the estimated degree of heterogeneity $\hat{\chi} = 2.1$ in statistics. To comprehensively evaluate the detection performance of the proposed method, it is compared with several state-of-the-art techniques, including: the generalized likelihood ratio test (GLRT) from [40], the magnitude-based method in multi-channel SAR-GMTI clutter suppression (see (7)), the dual-channel along-track interferometric magnitude from [35], the DPCA test from [37], the ATI-phase detection from [31], [45], [46], the joint metric of the interferometry magnitude and phase (IMP) from [36], the two-step methods combining the DPCA and ATI (DPCA+ATI) and the magnitude and ATI (Mag+ATI) from [37], and the optimal fusion-based method in [39].

TABLE I
SIMULATION PARAMETERS

Radar wavelength (λ)	**0.018 m**
Aircraft velocity (v_p)	**102 m/s**
Channel number (M)	**4**
Channel spacing (d)	**0.25 m**

To begin with, the simulation results of the compared tests with the target input SNR of 25 dB and radial velocity (v_r) of 2 m/s are shown in Fig. 8. The adaptive clutter suppression is performed on four-channel dataset with known target radial velocity for the GLRT, the Magnitude test and the proposed method, while the interferometric magnitude, the ATI phase, the IMP, and the DPCA are constructed with dual-channel dataset from channels 1 and 2. By comparing Figs. 8(a) and (b), it can be observed that most clutter can be effectively rejected in the multi-channel adaptive clutter suppression, although some strong clutter residuals present due to heterogeneous clutter. In Fig. 8(c), the interferometric magnitude method struggles to suppress the strong clutter, making it challenging to identify the true target with a low SCNR in the clutter background. For the GLRT in Fig. 8(d), the IMP in Fig. 8(f), and the DPCA test in Fig. 8(g), the target and some strong clutter both exhibit large values, potentially leading to false

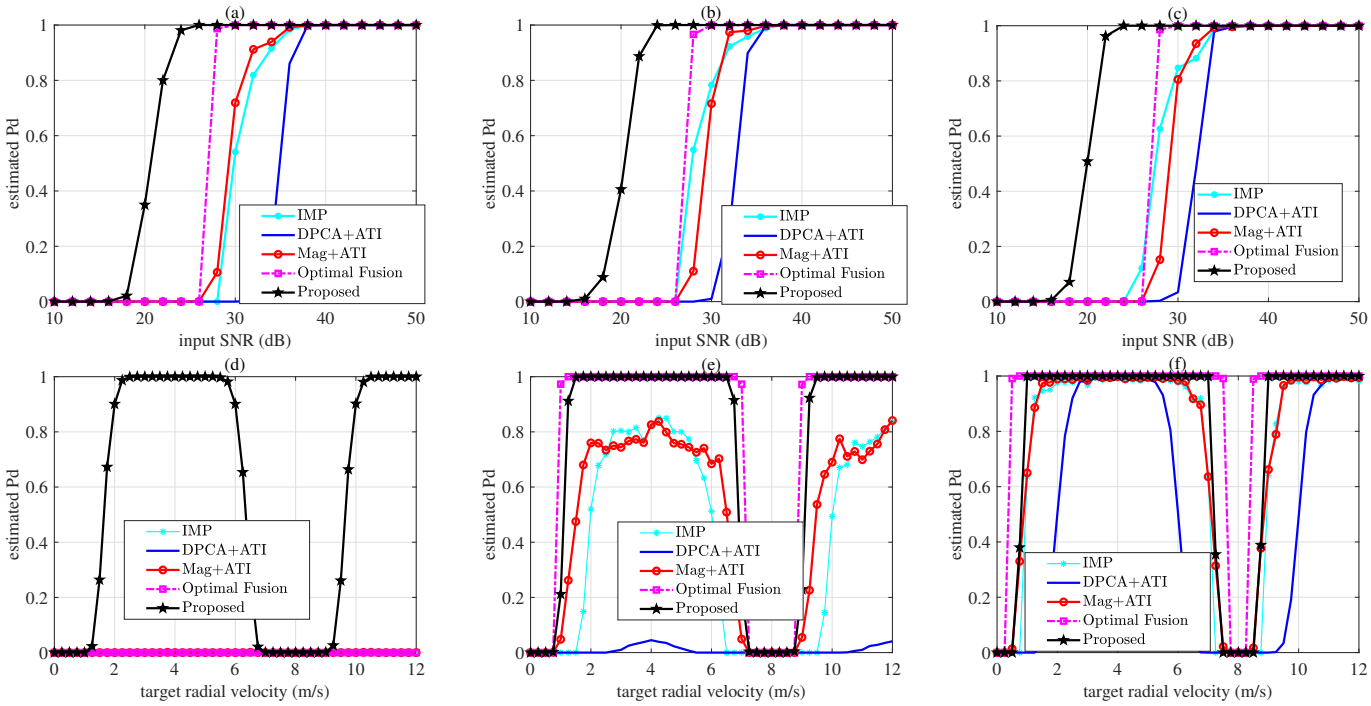

Fig. 10. ROC curves comparing the performance of different detection methods under $P_{\mathrm{f}} = 10^{-6}$ with $M = 4$
: (a) P_{d} versus input SNRs for $v_{\mathrm{r}} = 2$ m/s, (b) P_{d} versus input SNRs for $v_{\mathrm{r}} = 3$ m/s, (c) P_{d} versus input SNRs for $v_{\mathrm{r}} = 4$ m/s, (d) P_{d} versus v_{r} for an input SNR of 25 dB, (e)P_{d} versus v_{r} for an input SNR of 30 dB, and (f)P_{d} versus v_{r} for an input SNR of 35 dB, respectively.

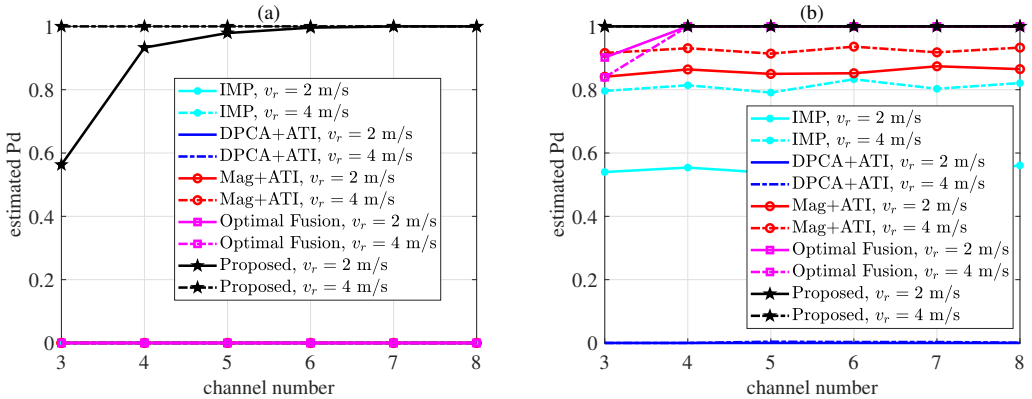

Fig. 11. P_{d} versus radar channel number M for the compared methods: (a) input SNR of 25 dB, and (b) input SNR of 30 dB, respectively.

alarms. In Fig. 8(e), the ATI phase of the target is relatively small, whereas the ATI phase for certain clutter seems to be large due to channel errors and random noise, which may result in degraded target detection performance. In contrast, the proposed test demonstrates significant improvement and most clutter can be effectively suppressed, making the true target stand out more prominently against the background.

Next, Monte Carlo simulation is employed to estimate the receiver operator characteristic (ROC) for the compared methods, where the Pfa (P_{f}) and Pd (P_{d}) are estimated by counting the numbers of the clutter cell and target cell exceeding the threshold, respectively. The ROC curves depicting Pd versus Pfa for the target with an input SNR of 25 dB and $v_{\mathrm{r}} = 2$ m/s are shown in Fig. 9(a), which demonstrate that the proposed method can achieve a higher Pd at low Pfas. The magnitude-based test (as in (7)) outperforms the DPCA test with two

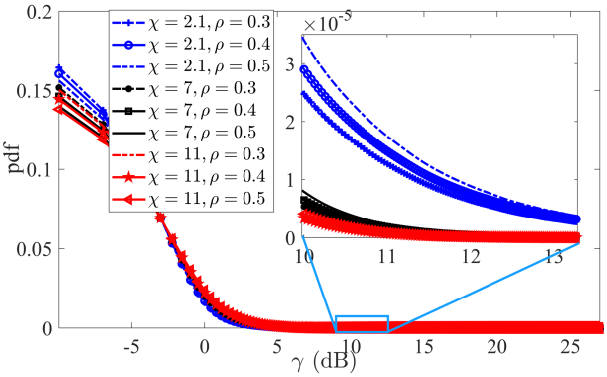

Fig. 12. Theoretical pdfs of γ with different parameters under H_0.

channels by increasing the spatial DoFs in clutter rejection,

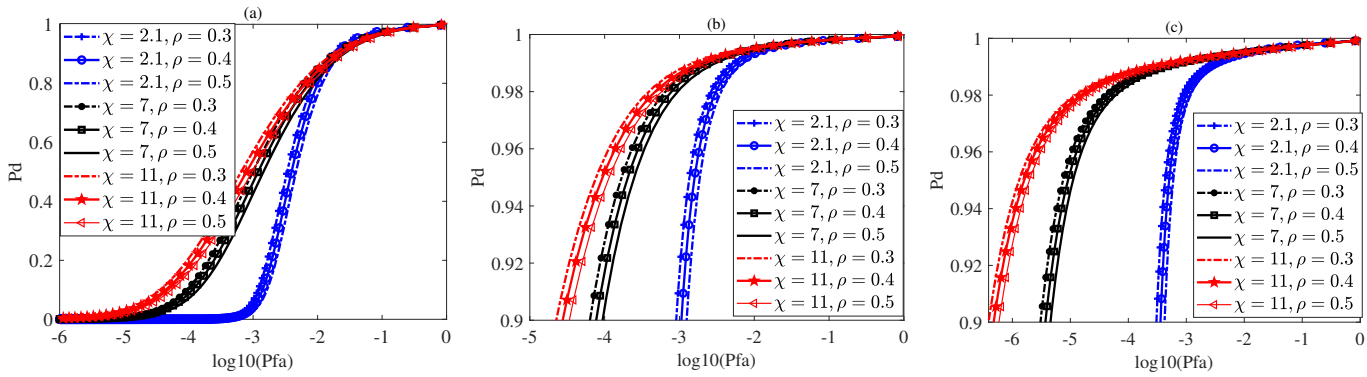

Fig. 13. $P_{\rm d}$ versus $P_{\rm f}$ for the proposed method versus different distribution parameters: (a) $\omega = 20$, $v_{\rm r} = 2$ m/s, (b) $\omega = 20$, $v_{\rm r} = 4$ m/s, and (c) $\omega = 100$, $v_{\rm r} = 2$ m/s, respectively.

and thus leads to a better Pd under the same Pfa. Furthermore, Fig. 9(a) indicates that the GLRT method struggles in the presence of isolated and strong clutter, as shown in Fig. 8(d), while both the interferometric magnitude (InMag) and ATI-phase test fail to adequately suppress clutter, showing poor target detection performance under low Pfas.

At a fixed Pfa, i.e., $P_{\rm f} = 10^{-6}$, we further compare the ROC of the proposed method with those of the IMP, the two-step detectors combining DPCA and ATI phase, the two-step detector based on the magnitude test and ATI phase, and the method by optimal fusion of the magnitude test and multi-baseline ATI-phase tests, respectively. For the two-step detectors, the Pfas for the magnitude and DPCA tests are both set to 10^{-5} in detection, followed by a Pfa of 10^{-1} for the ATI-phase test in the second detection. The ROC curves for $P_{\rm d}$ versus varying input SNRs with $v_{\rm r} = 2$ m/s, $v_{\rm r} = 3$ m/s and $v_{\rm r} = 4$ m/s are presented in Figs. 10(a), 10(b), and 10(c), respectively. Those ROC curves for $P_{\rm d}$ versus $v_{\rm r}$ with input SNRs at 25 dB, 30 dB, and 35 dB are shown in Figs. 10(d), 10(e), and 10(f), respectively. Seen from the ROC curves in Figs. 10(a), 10(b), and 10(c), the proposed method consistently has a higher Pd under the low input SNR, which can obtain a lower minimum discernible SCNR. Compared with the results in Fig. 10(d), the proposed method can achieve a smaller MDV, and shows significant advantages in detecting the dim targets with low SNRs within the heterogeneous clutter background. For high-speed targets when $v_{\rm r}$ exceeds the unambiguous velocity range ($[-3.78\text{m/s}, 3.78\text{m/s}]$), the ROC curves of the compared methods repeat in cycle, and the high-speed targets with $v_{\rm r}$ in blind-detection areas ($P_{\rm d} \ll 1$) will miss detection.

Furthermore, the ROC using different spatial DoF is estimated based on the above data. The $P_{\rm d}$ versus channel number M for the input SNRs of 25 dB and 30 dB are shown in Figs. 11(a) and 11(b), respectively. In Fig. 11(a), the proposed method has a higher Pd with larger M until achieves the max value 1. When the input SNR increases to 30 dB, as shown in Fig. 11(b), the Pd of the proposed method has already been 1, and thus, becomes insensitive to M. For the compared methods, as constructing the IMP, DPCA, and ATI tests only exploits dual-channel dataset, the detection performance is not sensitive to M. The magnitude test using multi-channel data in clutter suppression can be sensitive to M, and the two-step method by combining the magnitude and ATI tests outperforms the two-step method using DPCA and ATI tests owing to more spatial DoF. Additionally, with limited spatial DoF $M = 3$, as shown in Fig. 11, the proposed method may suffer from the performance loss for the target with a smaller SNR and a slower radial velocity, but it can still achieve significant performance improvements compared with mainstream methods.

Subsequently, the ROC sensitivity regarding the texture parameter χ and the correlation coefficient ρ between two clutter-suppression residuals is analyzed. Based on the statistics in (22), (24) and (30a), the theoretical pdfs of γ with the texture parameters $\chi \in \{2.1, 7, 11\}$ and residual correlation coefficients $\rho \in \{0.3, 0.4, 0.5\}$ under the hypothesis $\rm H_0$ are shown in Fig. 12. The smaller value of χ can represent a more heterogeneous clutter background. It can be seen from Fig. 12 that the distribution tails of γ at large values become heavier for the smaller χ and the larger ρ, which potentially result in a higher Pfa during target detection. With the pdfs and (23), (26), (31), and (32), the ROC curves of $P_{\rm d}$ versus $P_{\rm f}$ are depicted in Fig. 13, where Figs. 13 (a), 13 (b), and 13 (c) correspond to the targets with $\omega = 20$, $v_{\rm r} = 2$ m/s, $\omega = 20$, $v_{\rm r} = 4$ m/s, and $\omega = 100$, $v_{\rm r} = 2$ m/s, respectively. In the curves, the proposed method exhibits a higher Pd under the same Pfa for the larger χ and the smaller ρ, implying improved detection performance in a more homogeneous clutter background and with a lower corelation effect between the two clutter-suppression residuals.

B. Real-data Experiments

To evaluate the target detection performance of the proposed detector, we utilized the real data collected by an airborne four-channel X-band SAR with VV polarization that the vertical polarization is both transmitted and received by the radar in urban areas of China. Specifically, the aircraft flew with a velocity of approximately 102 m/s at the altitude about 510 m. A uniform linear array is installed along the aircraft's track direction, consisting of four sub-arrays (channels) with the spacing between adjacent channel being 0.25 m. During the data collection, the system operates in the side-looking mode to transmit the linear frequency modulation signals with the whole antenna aperture at a wavelength of 0.018 m, and then, receives the echoes from each channel individually. For the

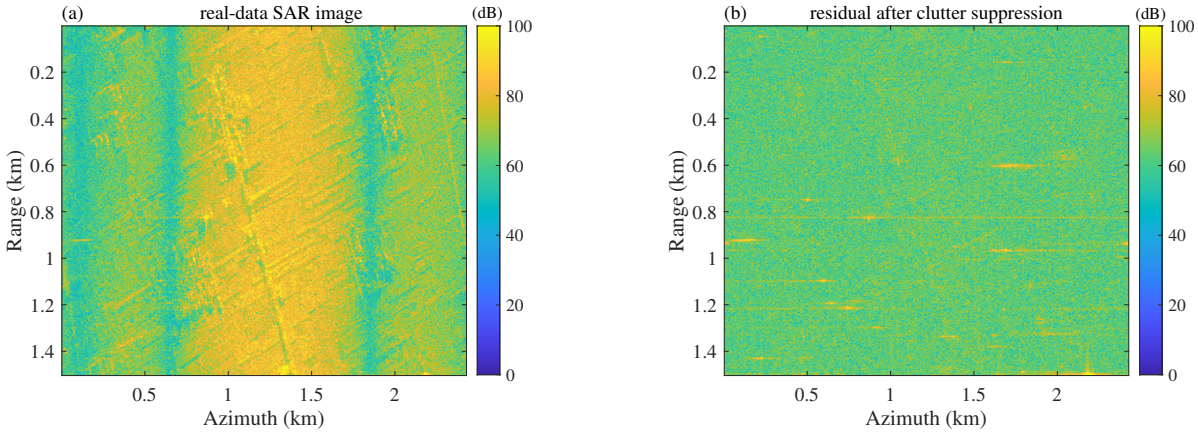

Fig. 14. Scenario: (a) the azimuth-range image and (b) the adaptive clutter suppression residual.

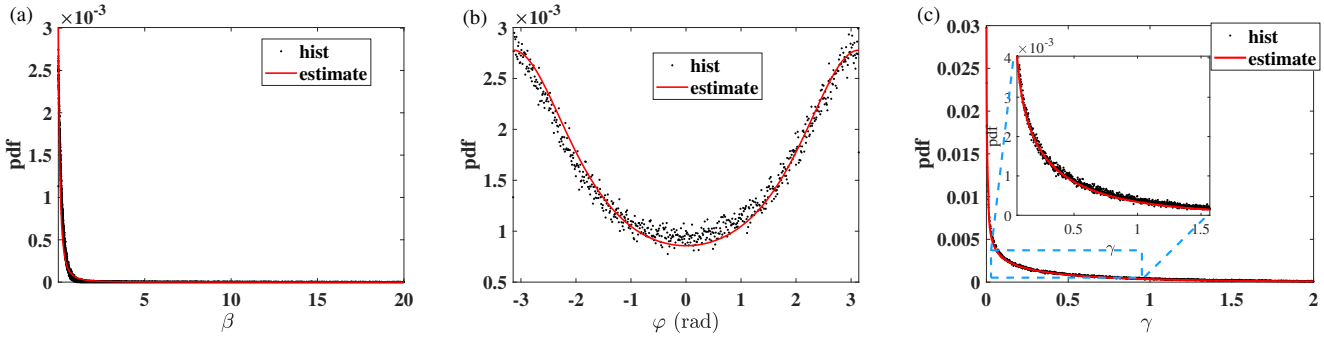

Fig. 15. Histogram and estimated pdfs: (a) β, (b) φ, and (c) γ.

dataset, the CPI contains 512 pulses with a pulse repetition frequency of 800 Hz. In data preprocessing, raw SAR data are subjected to imaging, channel coregistration and balancing as described in [3]. Then, four SAR images with a resolution of 3m $\times$ 3m in the range and azimuth directions are generated.

For the real-data clutter suppression, the clutter samples for estimating the CCM are selected based on the clutter interferometric phase similarity with the threshold of 0.1 rad (i.e., $<$ 0.1 rad), and the filter weights are constructed using the method in [50]. For the scenario, the azimuth-range images before and after clutter suppression are shown in Fig. 14(a) and Fig. 14(b), respectively. As observed in Fig. 14(b), most clutter has been effectively suppressed, although some strong residuals remain, which may represent potential moving targets or clutter. With all the residual samples, we estimate $\hat{\chi} = 2.1$ to ensure a root mean square error of 0.12×10^{-7} in statistical modeling, implying a high degree of environmental heterogeneity, and the histogram and estimated pdf under the hypothesis H_0 are shown in Fig. 15(a). On the other hand, two residuals obtained from clutter suppression, one from the afore-three-channel dataset and another from the after-three-channel dataset, respectively, are used to estimate the interferometric phase φ via (14), forming the basis of the proposed phase term in (19). With $\hat{\rho} \approx 0.38$ and $\varphi_{\mathrm{c}} = \pi$ based on two residuals, the statistics of φ is estimated by (24), and then the statistics of γ under the hypothesis H_0 are estimated using (30a). The histogram and estimated pdfs for φ and γ are shown in Figs. 15(b) and 15(c), respectively. It can be seen that the derived pdfs align with the measurements.

Next, the compared methods are performed with the same Pfa (10^{-6}) for target detection. Specifically, the local detection Pfas of the two-step detectors are set to 10^{-5} and 10^{-1}, respectively. As to the optimal fusion-based method, the auto-sensing process is first conducted with the constant target parameters, i.e., the MDV of 0.5 m/s, the minimum discernible SCNR of 10 dB, and a high overall Pfa of 10^{-4}, leading to 475 potential targets. Then, the cognitive detection is applied on the potential targets using the Pfa of 10^{-6}. Consider that the vehicle (in size of 2.8 m $\times$ 5 m in practice) would occupy one to two pixels. Based on the detected pixels in each compared method, the target pixel clustering based on the target radial velocity consistency and spatial distance is further applied for accurately obtaining each potential target. Additionally, given that moving targets exhibit shifts along the azimuth direction due to their non-zero radial velocities during the SAR imaging process, the detected targets are further relocated in the SAR images. This relocation is performed based on the relationship between the target radial velocity v_{r} and the azimuthal displacement $\triangle x$, expressed as $\triangle x = v_{\mathrm{r}} \times R / v_{\mathrm{p}}$, where R denotes the target slant range. The target detection, cluster and azimuth relocation results for the compared methods are shown in Fig. 16, where the detected targets are marked with red triangles, and their relocated locations in the SAR image are highlighted with green triangles. It is noted that some potential targets near the edges of the SAR images may fall outside the image boundaries following the relocation processing. Additionally, due to the lack of prior knowledge about ground moving targets in the SAR images, the relocated targets found on or

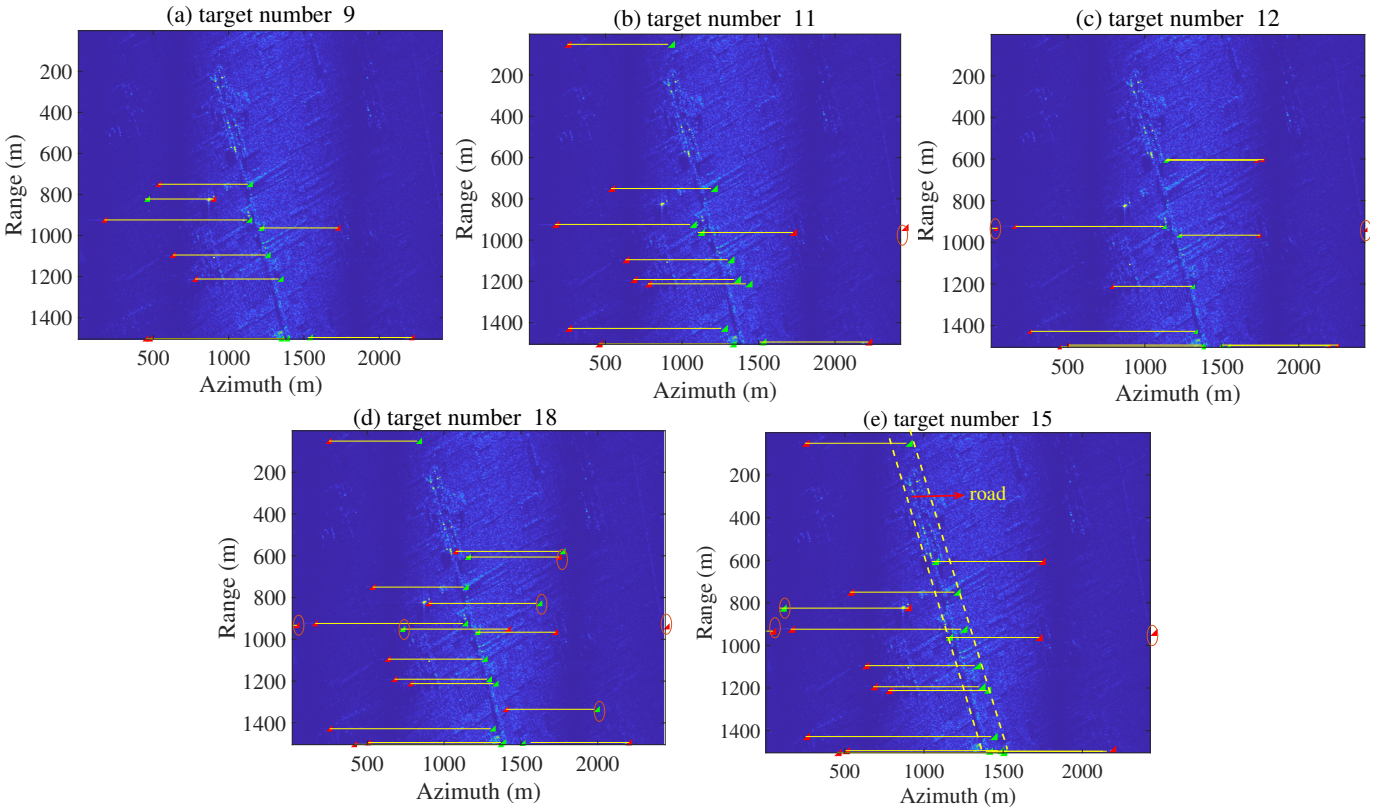

Fig. 16. The real-data target detection and relocation results for the compared methods under $P_{\mathrm{f}} = 10^{-6}$: (a) IMP, (b) two-step detector with DPCA and ATI tests, (c) two-step detector with the Magnitude and ATI tests, (d) optimal fusion-based method, and (e) the proposed method, respectively (Red triangle: detected target; Green triangle: related location).

TABLE II
COMPUTATIONAL TIME COMPARISONS

Method	Statistical Estimation	Total Detection
IMP	**1.6577 s**	**3.8456 s**
DPCA and ATI	**1.4956 s**	**3.7623 s**
Magnitude and ATI	**1.5067 s**	**4.1612 s**
Optimal fusion method	**114.3211 s**	**125.8273 s**
Proposed method	**21.2326 s**	**24.2121 s**

near roads (considering the relocation errors), are assumed to be true targets. In Figs. 16(a), 16(b), 16(c), 16(d), and 16(e), the potential targets are 9, 11, 12, 18, and 15 for the IMP, the two-step detection with DPCA and ATI tests, the two-step detection with magnitude and ATI tests, the optimal fusion-based detector, and the proposed method, respectively. It can be observed that miss detection of some potential targets occur in the first three methods under the Pfa of 10^{-6}. In the Figs. 16(d) and 16(e), where the detected targets away from roadways (marked with red circles) may be false alarms. Note that the proposed method can effectively detect the potential targets that are relocated near roadways, and detect fewer false alarms compared with the optimal fusion-based approach.

Based on the real SAR images, the computational complexities for the compared methods are estimated. The SAR image contains 501×512 pixels in range and azimuth plane, and the processing chain, including the data coregistration and balancing between channels, test construction, statistical estimation, and target detection, cluster and relocation, is performed in each method with Matlab R2021a on the DESKTOP-ULV6L48 (with 11th Gen Intel(R) Core(TM) i7-11800H at 2.30GHz and the random-access memory of 32 GB). The computational time of the statistical estimation and total detection process is recorded in second by Tab. II. It is observed that the optimal fusion method is most time-intensive, followed by the proposed method, while the IMP method and the two-step detectors consume less time. Specifically, the statistical estimation process in the proposed method requires slightly more time in the real-time processing.

Moreover, the ROC curves in the real-data clutter background are predicted by adding simulation targets. The targets are simulated based on the signal models in (2) and (3), and randomly added in the real-world clutter background. As the noise power is unknown in the real dateset, the target signal power is set according to the input SCNR, and the smaller input SCNR can reflect the more dense clutter case compared with the target. For each target, we repeat the simulation process for 1000 times, and then, evaluate the ROC of the compared methods. The target detection performance of the compared methods under $P_{\mathrm{f}} = 10^{-6}$ is shown in Fig. 17, where Figs. 17(a), 17(b), and 17(d) are the Pd versus input SCNRs for v_{r}=2 m/s, v_{r}=3 m/s, and v_{r}=4 m/s, respectively, while Figs. 17(d), 17(e), and 17(f) are the Pd versus target radial velocities for input SCNRs of 0 dB, 10 dB, and 25 dB, respectively. In Fig. 17, the output SCNRs of the simulated targets in the four-channel clutter suppression processing are shown by the right vertical axis. Based on the ROC curves, the MDV and minimum discernible input SCNR (for $P_{\mathrm{d}} \geq 0.95$)

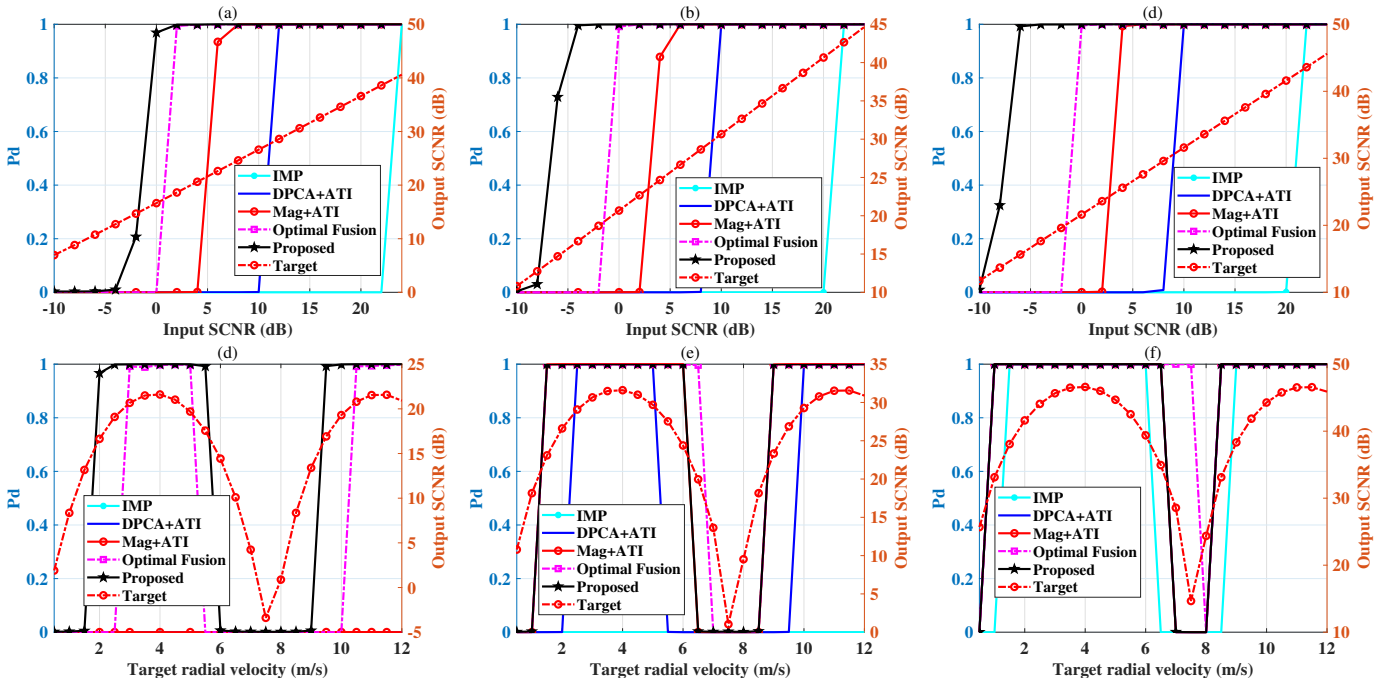

Fig. 17. ROC curves comparing the performance of different detection methods under $P_{\mathrm{f}} = 10^{-6}$: (a) P_{d} versus input SCNRs for $v_{\mathrm{r}} = 2$ m/s, (b) P_{d} versus input SCNRs for $v_{\mathrm{r}} = 3$ m/s, (c) P_{d} versus input SCNRs for $v_{\mathrm{r}} = 4$ m/s, (d) P_{e} versus v_{r} for an input SCNR of 0 dB, (e) P_{d} versus v_{r} for an input SCNR of 10 dB, and (f) P_{d} versus v_{r} for an input SCNR of 25 dB, respectively.

TABLE III
DETECTION PERFORMANCE COMPARISONS

Method	Minimum Discernible Input SCNR (dB)	MDV (m/s)
IMP	**25 (v_{r}: 2 m/s); 22 (v_{r}: 3 m/s); 20 (v_{r}: 4 m/s)**	**1 (input SCNR: 25 dB)**
DPCA and ATI	**12 (v_{r}: 2 m/s); 10 (v_{r}: 3 m/s); 10 (v_{r}: 4 m/s)**	**2.5 (input SCNR: 10 dB); 0.5 (input SCNR: 25 dB)**
Magnitude and ATI	**8 (v_{r}: 2 m/s); 6 (v_{r}: 3 m/s); 4 (v_{r}: 4 m/s)**	**1.5 (input SCNR: 10 dB); 0.5 (input SCNR: 25 dB)**
Optimal Fusion	**2 (v_{r}: 2 m/s); 0 (v_{r}: 3 m/s); 0 (v_{r}: 4 m/s)**	**2.5 (input SCNR: 0 dB); 1.5 (input SCNR: 10 dB); 0.5 (input SCNR: 25 dB)**
Proposed	**0 (v_{r}: 2 m/s); -4 (v_{r}: 3 m/s); -6 (v_{r}: 4 m/s)**	**2 (input SCNR: 0 dB); 1.5 (input SCNR: 10 dB); 0.5 (input SCNR: 25 dB)**

for the compared methods are recorded in Tab. III. It can be observed that the proposed method can obtain a smaller MDV and a smaller minimum discernible SCNR in comparisons. Thus, the results can reliably validate the effectiveness of the proposed method in practical applications and verify the significant advantages in GMTI over the compared methods.

V. CONCLUSION

For a M-channel synthetic aperture radar (SAR) operating in the side-looking mode for ground moving target identification (GMTI), this paper proposes a novel target detector that combines the magnitude output from M-channel SAR-image clutter suppression with the phase term derived through the interferometry between two residuals of the first $M-1$ and the last $M-1$ channels, respectively. By incorporating the interferometric phase information between these residuals, the proposed method enhances the target-to-background contrast compared to tests solely based on the magnitude in multichannel clutter suppression. Furthermore, under the product-model clutter and Gaussian noise background, an approximate statistics of the proposed detector are derived theoretically, and the constant false alarm ratio detection is formulated. According to the receiver operator characteristic, predicted based on simulations and experiments, the proposed method shows high robustness against the heterogeneous clutter background, and achieves improved minimum discernible velocity and minimum discernible signal-to-clutter-plus-noise ratio, compared to state-of-the-art methods. These detection performance improvements can provide significant advantages in detecting slow and weak targets in practice.

Additionally, from the experimental results for the computational complexity, the proposed method requires slightly more processing time to accurately estimate the test statistics for determining the detection threshold. Future work will focus on developing more efficient estimation technologies for the proposed test statistics and expanding its applications to a broader range of scenarios, including the marine environment and the aerial targets.

REFERENCES

[1] J. K. Jao, "Theory of synthetic aperture radar imaging of a moving target," *IEEE Transactions on Geoscience and Remote Sensing*, vol. 39, no. 9, pp. 1984–1992, 2001.

[2] D. Cerutti-Maori, I. Sikaneta, and C. H. Gierull, "Optimum SAR/GMTI processing and its application to the radar satellite RADARSAT-2 for traffic monitoring," *IEEE Transactions on Geoscience and Remote Sensing*, vol. 50, no. 10, pp. 3868–3881, 2012.

[3] D. Cerutti-Maori and I. Sikaneta, "A generalization of DPCA processing for multichannel SAR/GMTI radars," *IEEE Transactions on Geoscience and Remote Sensing*, vol. 51, no. 1, pp. 560–572, 2013.

[4] L. H. Anusha, R. Rajesh, R. Sharma, S. Varughese, N. S. Chaya, and K. George, "On the robustness of JDL-STAP algorithm for real-world effects," in *2016 IEEE Annual India Conference*, Bangalore, India, Dec. 2016, pp. 1–6.

[5] C. Shuxuan, J. Limin, X. Maosheng, W. Lideng, and Z. Pengbin, "Detection ground slow moving target by airborne along- and across-track interferometric SAR," in *Proceedings of 2011 IEEE CIE International Conference on Radar*, Chengdu, China, Oct. 2011, pp. 1623–1626.

[6] D. Kim, A. J. Park, U.-S. Suh, D. Goo, D. Kim, B. Yoon, W.-S. Ra, and S. Kim, "Accurate clutter synthesis for heterogeneous textures and dynamic radar environments," *IEEE Transactions on Aerospace and Electronic Systems*, vol. 58, no. 4, pp. 3427–3445, 2022.

[7] Z. Xin, G. Liao, Z. Yang, Y. Zhang, and H. Dang, "A deterministic sea-clutter space–time model based on physical sea surface," *IEEE Transactions on Geoscience and Remote Sensing*, vol. 54, no. 11, pp. 6659–6673, 2016.

[8] J. K. Jao, "Target signal-to-noise loss in multichannel SAR–GMTI clutter suppression," *IEEE Transactions on Aerospace and Electronic Systems*, vol. 59, no. 6, pp. 9463–9479, 2023.

[9] A. De Maio and D. Orlando, "A survey on two-stage decision schemes for point-like targets in Gaussian interference," *IEEE Aerospace and Electronic Systems Magazine*, vol. 31, no. 4, pp. 20–29, 2016.

[10] Z. Dai, P. Wang, H. Wei, and Y. Xu, "Adaptive detection with constant false alarm ratio in a non-Gaussian noise background," *IEEE Communications Letters*, vol. 23, no. 8, pp. 1369–1372, 2019.

[11] H. Xu, Z. Yang, S. He, M. Tian, G. Liao, and Y. Sun, "A generalized sample weighting method in heterogeneous environment for space-time adaptive processing," *Academic Press*, vol. 72, pp. 147–159, 2018.

[12] Y. Xiong, W. Xie, Y. Wang, W. Chen, and M. Hou, "Short-Range Nonstationary Clutter Suppression for Airborne KA-STAP Radar in Complex Terrain Environment," *IEEE Journal of Selected Topics in Applied Earth Observations and Remote Sensing*, vol. 18, pp. 2766–2776, 2025.

[13] Z. Wang, H. Chen, S. Xu, and M. Li, "Machine Learning-Aided Nonhomogeneity Detection Method for Airborne Radar," *IEEE Transactions on Radar Systems*, vol. 3, pp. 220–232, 2025.

[14] M. L. Honig and J. S. Goldstein, "Adaptive reduced-rank interference suppression based on the multistage wiener filter," *IEEE Transactions on Communications*, vol. 50, no. 6, pp. 986–994, 2016.

[15] K. Duan, H. Xu, H. Yuan, H. Xie, and Y. Wang, "Reduced-DOF Three-Dimensional STAP via Subarray Synthesis for Nonsidelooking Planar Array Airborne Radar," *IEEE Transactions on Aerospace and Electronic Systems*, vol. 56, no. 4, pp. 3311–3325, 2020.

[16] W. Zhang, R. An, N. He, Z. He, and H. Li, "Reduced dimension STAP based on sparse recovery in heterogeneous clutter environments," *IEEE Transactions on Aerospace and Electronic Systems*, vol. 56, no. 1, pp. 785–795, 2020.

[17] Z. Liao, K. Duan, Z. Qiu, X. Yang, and Y. Li, "Space-Time Adaptive Processing Based on Interpretable Multimodule Convolutional Neural Network," *IEEE Sensors Journal*, vol. 25, no. 7, pp. 12 347–12 360, 2025.

[18] D. Wang, T. Wang, W. Cui, and X. Zhang, "A Clutter Suppression Algorithm via Enhanced Sparse Bayesian Learning for Airborne Radar," *IEEE Sensors Journal*, vol. 23, no. 10, pp. 10 900–10 911, 2023.

[19] Y. Guo, G. Liao, J. Li, and T. Gu, "A clutter suppression method based on NSS-RPCA in heterogeneous environments for SAR-GMTI," *IEEE Transactions on Geoscience and Remote Sensing*, vol. 58, no. 8, pp. 5880–5891, 2020.

[20] K. Greenewald, E. Zelnio, and A. H. Hero, "Robust SAR STAP via kronecker decomposition," *IEEE Transactions on Aerospace and Electronic Systems*, vol. 52, no. 6, pp. 2612–2625, 2017.

[21] S. Venkatasubramanian, C. Wongkamthong, M. Soltani, B. Kang, S. Gogineni, A. Pezeshki, M. Rangaswamy, and V. Tarokh, "Toward Data-Driven STAP Radar," in *2022 IEEE Radar Conference*, New York City, NY, USA, March 2022, pp. 1–5.

[22] B. Zou, W. Feng, and H. Zhu, "Airborne Radar STAP Method Based on Deep Unfolding and Convolutional Neural Networks," *Electronics*, vol. 12, no. 14, 2023.

[23] K. Duan, H. Chen, W. Xie, and Y. Wang, "Deep learning for high resolution estimation of clutter angle-Doppler spectrum in STAP," *IET Radar, Sonar Navig.*, vol. 16, no. 2, pp. 193–207, 2022.

[24] C. Wang, J. Shi, Y. Zhou, X. Yang, Z. Zhou, S. Wei, and X. Zhang, "Semisupervised Learning-Based SAR ATR via Self-Consistent Augmentation," *IEEE Transactions on Geoscience and Remote Sensing*, vol. 59, no. 6, pp. 4862–4873, 2021.

[25] C. Li, L. Du, and Y. Du, "Semi-supervised sar atr based on contrastive learning and complementary label learning," *IEEE Geoscience and Remote Sensing Letters*, vol. 21, pp. 1–5, 2024.

[26] P. Ren, Z. Han, Z. Yu, and B. Zhang, "Confucius tri-learning: A paradigm of learning from both good examples and bad examples," *Pattern Recognition*, vol. 163, no. 111481, pp. 1–14, 2025.

[27] B. Ge, D. An, J. Liu, D. Feng, L. Chen, and Z. Zhou, "Modified Adaptive 2-D Calibration Algorithm for Airborne Multichannel SAR-GMTI," *IEEE Geoscience and Remote Sensing Letters*, vol. 20, pp. 1–5, 2023.

[28] J. K. Jao, "Airborne GMTI clutter suppression performance utilizing a wideband sparse array," in *2013 IEEE International Symposium on Phased Array Systems and Technology*, Waltham, MA, USA, Oct. 2013, pp. 359–366.

[29] M. Weiss, "Analysis of some modified cell-averaging CFAR processors in multiple-target situations," *IEEE Transactions on Aerospace and Electronic Systems*, vol. AES-18, no. 1, pp. 102–114, 1982.

[30] F. Bandiera, D. Orlando, and G. Ricci, "One- and two-stage tunable receivers*," *IEEE Transactions on Signal Processing*, vol. 57, no. 8, pp. 3264–3273, 2009.

[31] C. H. Gierull, "Closed-form expressions for InSAR sample statistics and its application to non-Gaussian data," *IEEE Transactions on Geoscience and Remote Sensing*, vol. 59, no. 5, pp. 3967–3980, 2021.

[32] A. Budillon, C. H. Gierull, V. Pascazio, and G. Schirinzi, "Along-track interferometric SAR systems for ground-moving target indication: Achievements, potentials, and outlook," *IEEE Geoscience and Remote Sensing Magazine*, vol. 8, no. 2, pp. 46–63, 2020.

[33] S. Anand, D.-J. Kim, J.-H. Hwang, and J. Song, "Implementation of ATI-GMTI process on Airborne and Automobile SAR data," in *2021 7th Asia-Pacific Conference on Synthetic Aperture Radar (APSAR)*, Bali, Indonesia, Nov. 2021, pp. 1–5.

[34] Y.-G. Kang, S. Park, E. Kim, J.-U. Lee, K. Kim, S. Kim, and S.-O. Park, "Ground-Moving Target Indication Using Along Track SAR Interferometer Designed with Triangular Frequency-Modulated Continuous Wave Radar," *IEEE Transactions on Instrumentation and Measurement*, pp. 1–13, 2025.

[35] C. Gierull, "Statistical analysis of multilook SAR interferograms for CFAR detection of ground moving targets," *IEEE Transactions on Geoscience and Remote Sensing*, vol. 42, no. 4, pp. 691–701, 2004.

[36] G. Gao and G. Shi, "The CFAR detection of ground moving targets based on a joint metric of SAR interferogram's magnitude and phase," *IEEE Transactions on Geoscience and Remote Sensing*, vol. 50, no. 9, pp. 3618–3624, 2012.

[37] C. H. Gierull, I. Sikaneta, and D. Cerutti-Maori, "Two-step detector for RADARSAT-2's experimental GMTI mode," *IEEE Transactions on Geoscience and Remote Sensing*, vol. 51, no. 1, pp. 436–454, 2013.

[38] B. Liu, K. Yin, Y. Li, F. Shen, and Z. Bao, "An improvement in multichannel SAR-GMTI detection in heterogeneous environments," *IEEE Transactions on Geoscience and Remote Sensing*, vol. 53, no. 2, pp. 810–827, 2015.

[39] M. Tian and B. Liao, "Optimal Fusion-Based Target Detection With Multichannel ATI SAR," *IEEE Transactions on Geoscience and Remote Sensing*, vol. 62, pp. 1–15, 2024.

[40] A. Budillon, A. Evangelista, and G. Schirinzi, "GLRT detection of moving targets via multibaseline along-track interferometric SAR systems," *IEEE Geoscience and Remote Sensing Letters*, vol. 9, no. 3, pp. 348–352, 2012.

[41] H. Huang, S. Zhu, X. He, X. Li, and G. Liao, "A motion target refocusing method based on range frequency difference processing without parameter search," *IEEE Transactions on Geoscience and Remote Sensing*, vol. 63, pp. 1–18, 2025.

[42] B. Liu, T. Wang, Y. Li, F. Shen, and Z. Bao, "Effects of Doppler aliasing on baseline estimation in multichannel SAR-GMTI and solutions to address these effects," *IEEE Transactions on Geoscience and Remote Sensing*, vol. 52, no. 10, pp. 6471–6487, 2014.

[43] F. Robey, D. Fuhrmann, E. Kelly, and R. Nitzberg, "A CFAR adaptive matched filter detector," *IEEE Transactions on Aerospace and Electronic Systems*, vol. 28, no. 1, pp. 208–216, 1992.

[44] W. Yifeng, W. Tong, W. Jianxin, and D. Jia, "Robust training samples selection algorithm based on spectral similarity for space–time adaptive

processing in heterogeneous interference environments," *Radar Sonar and Navigation Iet*, vol. 9, no. 7, pp. 778–782, 2015.
[45] J.-S. Lee, K. Hoppel, S. Mango, and A. Miller, "Intensity and phase statistics of multilook polarimetric and interferometric SAR imagery," *IEEE Transactions on Geoscience and Remote Sensing*, vol. 449, pp. 567–589, 1994.
[46] R. J. A. Tough, D. Blacknell, and S. Quegan, "A statistical description of polarimetric and interferometric synthetic aperture radar data," *Proceedings of the Royal Society A: Mathematical, Physical and Engineering Sciences*, vol. 32, no. 5, pp. 1017–1028, 1995.
[47] B. X. Chen, W. Zhu, G. C. Sun, and L. Yang, *Mordern radar system analysis and design*. Xidian University Press, Xi'an, China, 2012.
[48] A. T. James, "Distributions of matrix variates and latent roots derived from normal samples," *Ann. Math. Statist.*, vol. 35, no. 2, pp. 475–501, 1964.
[49] S. Gao and H. Liu, "Performance Comparison of Statistical Models for Characterizing Sea Clutter and Ship CFAR Detection in SAR Images," *IEEE Journal of Selected Topics in Applied Earth Observations and Remote Sensing*, vol. 15, pp. 7414–7430, 2022.
[50] R. Lorenz and S. Boyd, "Robust minimum variance beamforming," *IEEE Transactions on Signal Processing*, vol. 53, no. 5, pp. 1684–1696, 2005.

Min Tian received the B.Eng. degree from Nanchang Hangkong University, Nanchang, China, in 2014, and the Ph.D. degree from Xidian University, Xi'an, China, in 2019. From 2019 to 2022, she was a Research Assistant in Xi'an Institution of Space Radio Technology, Xi'an, China. From 2022 to 2024, she was a Research Assistant in the Hangzhou Institution of Technology, Xidian University, Hangzhou, China.

She is currently an associate researcher in the Hangzhou Institution of Technology, Xidian University, Hangzhou, China. Her research interests include radar clutter simulation and characterization, adaptive signal processing and detection.

Bin Liao (Senior Member, IEEE) received the B.Eng. and M.Eng. degrees from Xidian University, Xi'an, China, in 2006 and 2009, respectively, and the Ph.D. degree from the University of Hong Kong, Hong Kong, in 2013. From 2013 to 2014, he was a Research Assistant with the Department of Electrical and Electronic Engineering, the University of Hong Kong, where he was also a Research Scientist with the Department of Electrical and Electronic Engineering from August to October 2016. From March to June 2023, he was a Visiting Professor with the Centre for Wireless Innovation (CWI), Queen's University Belfast, U.K. He is currently a Full Professor with the College of Electronics and Information Engineering, Shenzhen University, Shenzhen, China. His research interests include sensor array processing, adaptive filtering, and convex optimization, with applications to radar, navigation, and communications.

Dr. Liao was a recipient of the Best Paper Award in 2016 21st International Conference on Digital Signal Processing and 2017 22nd International Conference on Digital Signal Processing. He was a recipient of the National Natural Science Foundation of China and European Research Council (NSFC-ERC) programme. He is an Associate Editor of IEEE TRANSACTIONS ON AEROSPACE AND ELECTRONIC SYSTEMS, and Multidimensional Systems and Signal Processing.

Bo Yuan (Senior Member, IEEE) received the B.E. degree in Computer Science from the Nanjing University of Science and Technology, Nanjing, China, in 1998, and the M.Sc. and Ph.D. degrees in Computer Science from the University of Queensland (UQ), St Lucia, QLD, Australia, in 2002 and 2006, respectively. From 2006 to 2007, he worked as a Research Officer on a project funded by the Australian Research Council at UQ. From 2007 to 2021, he was a Faculty Member with the Division of Informatics, Tsinghua Shenzhen International Graduate School, Shenzhen, China, where he served as a Lecturer (2007–2009) and Associate Professor (2009–2021). During this period, he also held the role of Deputy Director of the Office of Academic Affairs (2013–2020).

He has authored more than 140 papers in refereed international conferences and journals. His research interests include data science, evolutionary computation, and intelligent decision making.

Denghui Hu is an Associate Researcher in the Innovation Academy for Microsatellites of Chinese Academy of Science. His main research directions include satellite system design, Carbon Dioxide Monitoring, and on-board intelligent processing.